

PREPARED FOR SUBMISSION TO JHEP

Dynamical scotogenic generation of the Linear and Inverse seesaws

Asmaa Abada,^a A. E. Cárcamo Hernández^{b,c,d} Salvador Urrea^a

^a*Pôle Théorie, Laboratoire de Physique des 2 Infinis Irène Joliot-Curie (UMR 9012), CNRS/IN2P3, 15 Rue Georges Clemenceau, 91400 Orsay, France*

^b*Universidad Técnica Federico Santa María, Casilla 110-V, Valparaíso, Chile*

^c*Centro Científico-Tecnológico de Valparaíso, Casilla 110-V, Valparaíso, Chile*

^d*Millennium Institute for Subatomic Physics at the High-Energy Frontier, SAPHIR, Chile*

E-mail: asmaa.abada@ijclab.in2p3.fr, antonio.carcamo@usm.cl, salvador.urrea@ijclab.in2p3.fr

ABSTRACT: We propose an economical model in which the tiny active neutrino masses arise from an interplay of linear and inverse seesaw mechanisms. The Standard Model is extended by a local $U(1)'$ gauge symmetry and discrete $\mathbb{Z}_3 \otimes \mathbb{Z}_4$ symmetries, together with gauge-singlet scalars and neutral leptons. Owing to the preserved discrete symmetries after spontaneous symmetry breaking, the linear and inverse seesaw mechanisms are dynamically generated at the two-loop level, while the same symmetries ensure the stability of both scalar and fermionic dark matter candidates. One of the distinctive features of the model is a fermionic dark matter candidate whose mass is generated at one loop, whereas scalar dark matter masses arise at tree level. The model satisfies current constraints from neutrino oscillation data, dark matter direct detection, invisible Higgs decays, Z' searches, and charged lepton flavor violation, in addition we also discuss predictions for muonium states. The outcome of our analysis is that the inverse seesaw contribution dominates over the linear one, suggesting that atmospheric neutrino mass squared splitting arises from the inverse seesaw mechanism, whereas the solar one is generated from the linear seesaw. Finally, our model offers an explanation of the hierarchy between the atmospheric and solar neutrino mass squared splittings, in addition to the smallness of active neutrino masses, feature not presented in many low-scale seesaw models. In addition, our parameter-space scan shows a slight preference for the normal neutrino mass ordering.

KEYWORDS: Neutrino mass generation mechanisms, dynamical generation of low-scale seesaw, inverse and linear seesaw, scotogenic model

Contents

1	Introduction	1
2	The scotogenic LISS model	4
2.1	Symmetries and particles	4
2.2	The scalar potential	7
2.3	Anomaly, stability and unitarity conditions	10
3	Neutrino mass generation	10
3.1	Generation of the LISS mechanism	11
3.2	Majorana mass generation for the dark neutral leptons Ψ_R and $\tilde{\Psi}_R$	14
4	Phenomenology	14
4.1	Collider searches	14
4.2	Charged lepton flavor violation	16
4.2.1	Radiative cLFV decays	16
4.2.2	CR($\mu - e, N$)	17
4.2.3	$l_\alpha \rightarrow l_\beta l_\beta l_\rho$	18
4.3	Muonium decays and Muonium-antimuonium oscillation	19
5	Results	20
6	Conclusions	24
A	Anomaly Cancellation	26
B	Stability and unitarity conditions	27
C	Loop Functions and Form Factors	31
D	One-Loop LFV Higgs Yukawa and Matching to Scalar Operators	33

1 Introduction

The existence of dark matter and neutrino oscillation phenomena are strong indications of beyond Standard Model (BSM) physics, as the Standard Model (SM) provides neither a dark matter candidate nor a mechanism for generating active neutrino masses. The

connection between the dark matter problem and the tiny active neutrino masses, together with the observed lepton mixing, offers an interesting and challenging avenue to explore.

While a minimal extension of the SM that introduces right-handed Majorana neutrinos (ν_R) can generate active neutrino masses via the seesaw mechanism [1–7], accommodating sub-eV neutrino masses [8] requires, in the canonical type-I seesaw realization, either a high lepton-number-violating (LNV) scale or tiny Yukawa couplings if implemented at low scale. In either case, the phenomenology of this mechanism is extremely suppressed. The resulting mixing between active and heavy neutrinos is very small, leading to rates for charged lepton flavor-violating (cLFV) processes that are far below current experimental sensitivity. An alternative that allows for large Yukawa couplings with a comparatively low seesaw scale is to introduce additional sterile fermions together with an approximate lepton number symmetry. This is the case in the inverse seesaw (ISS) [9–15] or the linear seesaw (LSS) [16, 17] realizations.

Additionally, to generate tree-level Majorana masses for the active neutrinos, low-scale seesaw models introduce a new scale that explicitly breaks lepton number symmetry, either through a Majorana mass term (as in the ISS) or via an additional Yukawa interaction for the new fermion singlets (as in the LSS). In these scenarios, the LNV parameters are *ad hoc* and are assumed to be small, a hypothesis that, despite being technically natural and therefore stable under radiative corrections, lacks a more fundamental motivation. Possible explanations for the origin of these small LNV parameters have been proposed in several models [18–48].

In this work we explore the possibility of explaining the origin of the tiny masses of the active neutrinos (and the lepton mixing matrix) from the interplay of both linear and inverse seesaw mechanisms. The associated small LNV couplings of the LSS and ISS are dynamically generated at the two-loop level, which naturally justifies their smallness. In the model we propose, the SM gauge sector is extended by a local $U(1)'$ symmetry and by discrete $\mathbb{Z}_3 \otimes \mathbb{Z}_4$ symmetries, while the particle content is enlarged with SM-gauge-singlet scalars and neutral leptons. A key feature of the model is the dynamical generation of the LNV parameters of the LSS and ISS mechanisms at two-loop level, arising from the spontaneous breaking of the local $U(1)'$ and the \mathbb{Z}_4 symmetries. This setup provides viable DM candidates, originating either from the sterile neutrino sector or from the extended scalar sector, which are in fact the particles responsible for generating both the inverse and linear seesaw mechanisms.

Many extensions of the SM that propose a radiative mass generation for the (new) neutral Majorana lepton masses rely on a preserved discrete symmetry that prevents tree-level mass contributions but allows them to appear at loop level [49–81]. These models naturally link dark matter and neutrino mass generation. In most cases, neutrino masses arise at one loop, which often necessitates either tiny Yukawa couplings, comparable to that

of the electron, or very small mass splittings between the CP-even and CP-odd components of the scalar seesaw mediators.

On the other hand, models featuring linear [64, 82–86] or inverse [10, 14, 15, 17–20, 31, 35, 37, 38, 41–45, 47, 87–90] seesaw mechanisms for the generation of light (active) neutrino masses offer an interesting and testable explanation for their smallness. These models provide sizeable active–heavy neutrino mixings, allowing cLFV processes to occur at rates within experimental reach, making linear and inverse seesaw constructions testable in cLFV experiments. Furthermore, when radiative mechanisms are implemented in linear and/or inverse seesaw models, the resulting scotogenic scenarios establish a connection between dark matter and neutrino mass generation, as some neutral seesaw messengers can serve as dark matter candidates. Their stability is ensured by discrete symmetries, which are also essential for the implementation of radiative seesaw mechanisms. Dark matter candidates in these models can annihilate into pairs of SM particles or other BSM states, successfully reproducing the observed dark matter relic abundance within suitable regions of parameter space. In addition, models embedding linear and inverse seesaw mechanisms can provide a viable framework for resonant leptogenesis due to the small mass splitting between the heavy pseudo-Dirac neutral leptons, since the physical heavy neutrinos form pseudo-Dirac pairs with a mass gap proportional to the small LNV parameters. All these arguments add up to reinforce the motivation to find a minimalist but testable scenario that can solve these problems with the same Lagrangian interactions.

In more detail, our model consists of an extension of the Inert Doublet Model, where the tiny masses of the active neutrinos are generated from an interplay of linear and inverse seesaw mechanisms—referred to as “LISS”—both generated at the two-loop level. The SM gauge symmetry is augmented by the inclusion of a local $U(1)'$ and the discrete symmetries $\mathbb{Z}_3 \otimes \mathbb{Z}_4$, while the SM particle content is enlarged by several gauge-singlet scalars and neutral leptons. The local $U(1)'$ and the \mathbb{Z}_4 symmetries are spontaneously broken, whereas the \mathbb{Z}_3 symmetry remains exact. We assume that the $U(1)'$ is spontaneously broken down to a residual \mathbb{Z}_2 discrete symmetry, the preserved $\mathbb{Z}_2 \times \mathbb{Z}_3$ symmetries being essential to ensure the radiative nature of the linear and inverse seesaw mechanisms at the two-loop level. Under these assumptions, our model is anomaly-free, both gauge and gravitational. In addition to dynamically generating the LISS and thus small masses for the active neutrinos, our model provides a scotogenic origin for the LNV parameters of the ISS and LSS. The model therefore supplies two dark matter candidates, one scalar and one fermionic, both stable thanks to the residual $\mathbb{Z}_2 \times \mathbb{Z}_3$ symmetry. A notable feature is the difference in their mass generation. The fermionic candidate, identified as the lightest neutral lepton carrying a non-trivial \mathbb{Z}_3 charge, acquires mass radiatively at the one-loop level. All scalar dark matter masses, in contrast, arise at tree level. It yields sizeable rates for cLFV observables and among these, we evaluate the contributions to the decay rates of $\ell_\alpha \rightarrow \ell_\beta \ell_\beta \ell_\rho$, and

to the radiative processes $\mu \rightarrow e\gamma$, $\tau \rightarrow \mu\gamma$, and $\tau \rightarrow e\gamma$, as well as muon–electron conversion in nuclei, $\text{CR}(\mu - e, \text{N})$. We furthermore study the impact of our model on the muonium (Mu) state, including cLFV decays and muonium–antimuonium oscillations, providing predictions and a phenomenological analysis. We already anticipate highlighting that in this scenario, the constraint from neutrino data on lepton mixing implies that the dominant contribution to the cLFV amplitudes (boxes and penguins) is essentially due to the scalar sector. Furthermore, in the fermionic DM scenario, constraints arising from the LUX experiment [91] set the ratio $\frac{M_{Z'}}{g_X}$ to be larger than about 40 TeV for a 10 GeV fermionic dark matter mass.

The paper is organized as follows: in Section 2 we provide a detailed description of the model with its symmetries and field content. We also discuss the stability condition of the scalar potential and its consequences. The dynamical generation of the complete mass matrix of the neutral leptons at the two-loop level is derived in Section 3; the generation of active light neutrino masses and the lepton mixing is also detailed in this section. Section 4 is devoted to the phenomenological study of our model with high-intensity observables, mainly cLFV ones, collider searches, as well as current constraints. For this, we present a detailed calculation of the observables we consider. Our results are presented and discussed in Section 5. We finally summarize our findings in Section 6. The Appendices provide supplementary details on anomaly cancellation, the stability and unitarity conditions of the model, and the explicit form factors for cLFV observables.

2 The scotogenic LISS model

In this section, we present the two-loop level scotogenic inverse and linear seesaw model we propose.

2.1 Symmetries and particles

The model corresponds to a minimal extension of the inert doublet model, where the scalar field content is augmented by the inclusion of the gauge singlet fields φ , ξ , χ , ρ , σ and the fermion sector is enlarged with Majorana neutrinos ν_R , N_R , Ψ_L , Ψ_R and $\tilde{\Psi}_R$, and heavy Dirac neutral leptons Ω_R , Ω_L . Regarding the gauge group, we extend the SM with a local $U(1)'$ and discrete $\mathbb{Z}_3 \otimes \mathbb{Z}_4$ symmetries. The scalar potential of our model yields a tree-level instability forming vacuum expectation values (VEVs) of $\langle \phi \rangle = v_\phi$, being ϕ the SM Higgs doublet, $\langle \sigma \rangle = v_\sigma$, $\langle \rho \rangle = v_\rho$ that trigger the following spontaneous symmetry

breaking (SSB) pattern:

$$SU(3)_C \otimes SU(2)_L \otimes U(1)_Y \otimes U(1)' \otimes \mathbb{Z}_3 \otimes \mathbb{Z}_4 \quad (2.1)$$

$$\Downarrow v_\sigma, v_\rho$$

$$SU(3)_C \otimes SU(2)_L \otimes U(1)_Y \otimes \underbrace{\tilde{\mathbb{Z}}_6}_{\text{remnant of } U(1)'} \otimes \mathbb{Z}_3 \otimes \underbrace{\mathbb{Z}_2}_{\mathbb{Z}_4 \rightarrow \mathbb{Z}_2} \quad (2.2)$$

$$\Downarrow v_\phi$$

$$SU(3)_C \otimes U(1)_{\text{em}} \otimes \tilde{\mathbb{Z}}_6 \otimes \mathbb{Z}_3 \otimes \mathbb{Z}_2, \quad (2.3)$$

After spontaneous symmetry breaking, the local $U(1)'$ symmetry is spontaneously broken down to a conserved $\tilde{\mathbb{Z}}_6$ discrete group which has as subgroup the preserved matter parity $\tilde{\mathbb{Z}}_2 \subset \tilde{\mathbb{Z}}_6$ symmetry with the $\tilde{\mathbb{Z}}_2$ charges of the fields defined as $(-1)^{3Q_{U(1)'}+2s}$, where $Q_{U(1)'}$ is the charge under $U(1)'$ and s is the spin of the particle¹. Finally, the \mathbb{Z}_4 is broken to another independent preserved \mathbb{Z}_2 symmetry. The charge assignments under the extended $SU(3)_C \otimes SU(2)_L \otimes U(1)_Y \otimes U(1)' \otimes \mathbb{Z}_3 \otimes \mathbb{Z}_4$ gauge group and the residual $\tilde{\mathbb{Z}}_2$ symmetry for all particles of the model are provided in Table 1.

Field	q_{iL}	u_{iR}	d_{iR}	l_{iL}	l_{iR}	ν_R	N_R	Ψ_L	Ψ_R	$\tilde{\Psi}_R$	Ω_L	Ω_R	ϕ	η	φ	ξ	χ	σ	ρ
$SU(3)_C$	3	3	3	1	1	1	1	1	1	1	1	1	1	1	1	1	1	1	1
$SU(2)_L$	2	1	1	2	1	1	1	1	1	1	1	1	2	2	1	1	1	1	1
$U(1)_Y$	$\frac{1}{6}$	$\frac{2}{3}$	$-\frac{1}{3}$	$-\frac{1}{2}$	-1	0	0	0	0	0	0	0	$\frac{1}{2}$	$-\frac{1}{2}$	0	0	0	0	0
$U(1)'$	$\frac{1}{3}$	$\frac{1}{3}$	$\frac{1}{3}$	-1	-1	-1	1	1	-1	-1	-2	-2	0	0	0	-1	3	2	0
\mathbb{Z}_3	0	0	0	0	0	0	0	1	1	0	-1	-1	0	-1	1	1	-1	0	0
\mathbb{Z}_4	0	0	0	0	0	0	0	0	0	1	1	1	0	0	0	1	-1	2	2
$\tilde{\mathbb{Z}}_6$	1	1	1	3	3	3	3	3	3	3	0	0	0	0	0	3	3	0	0
$\tilde{\mathbb{Z}}_2$	0	0	0	0	0	0	0	0	0	0	1	1	0	0	0	1	1	0	0
\mathbb{Z}_2	0	0	0	0	0	0	0	0	0	1	1	1	0	0	0	1	1	0	0

Table 1: Particle charge assignments under $SU(3)_C \times SU(2)_L \times U(1)_Y \times U(1)' \times \mathbb{Z}_3 \times \mathbb{Z}_4$ and the residual discrete symmetries after spontaneous breaking. The model itself is summarized on the 6 first rows of the table. Here $i = 1, 2, 3$ and for completeness $\tilde{\mathbb{Z}}_6$ is the remnant of $U(1)'$, $\tilde{\mathbb{Z}}_2$ is its matter-parity subgroup, and \mathbb{Z}_2 is the subgroup preserved after \mathbb{Z}_4 breaking.

The spontaneous breaking of the $U(1)'$ and \mathbb{Z}_2 symmetries occurs at the TeV scale, triggered by the vacuum expectation values (VEVs) of the scalar fields σ and ρ , respectively.

¹Strictly speaking, the charge assignment for the preserved subgroup $\tilde{\mathbb{Z}}_2 \subset \tilde{\mathbb{Z}}_6$ is $(-1)^{3Q_{U(1)'}}$. However, Lorentz invariance ensures that only an even number of fermionic fields can appear in operators, making both assignments physically equivalent.

The other scalar fields η , ξ , χ , and φ , which carry non-trivial charges under $\tilde{\mathbb{Z}}_2 \otimes \mathbb{Z}_3$, do not acquire VEVs. This ensures that the $\tilde{\mathbb{Z}}_2 \otimes \mathbb{Z}_3$ symmetry remains exact. Preserving this symmetry is essential both to guarantee the radiative origin of the linear and inverse seesaw mechanisms and to ensure the stability of the scalar and fermionic dark matter candidates.

Regarding the dynamical generation of lepton number violation, the one-loop radiative linear and inverse seesaw mechanisms are forbidden by the symmetries of the model implying the absence of tree-level Dirac and Majorana mass terms. In particular, the Dirac mass term $M_{\Psi}^D \bar{\Psi}_L \Psi_R$ and the Majorana mass term $M_{\Psi}^M \Psi_R \bar{\Psi}_R^C$ are both absent: the Majorana term is forbidden by the local $U(1)'$ symmetry, whereas the Dirac term is excluded by the \mathbb{Z}_3 symmetry. In other words, these terms cannot be generated dynamically at tree level because the Yukawa couplings $\bar{\Psi}_L \sigma \Psi_R$ and $\Psi_R \sigma \bar{\Psi}_R^C$ are not invariant under $U(1)'$ and are simultaneously forbidden by the \mathbb{Z}_3 and \mathbb{Z}_4 symmetries. Consequently, the preserved \mathbb{Z}_3 and \mathbb{Z}_4 symmetries play a crucial role in preventing one-loop active neutrino masses from arising through the linear and inverse seesaw mechanisms.

Moreover, both $U(1)'$ and \mathbb{Z}_4 forbid the Yukawa interaction $N_R \sigma \bar{N}_R^C$, which would otherwise induce a tree-level inverse seesaw contribution. It is important to note that the Majorana mass term

$M_{\Psi} \Psi_R \bar{\Psi}_R^C$ only appears at the one-loop level, generated via the virtual exchange of the Majorana leptons Ω_R together with the real and imaginary components of the singlet scalars ξ and χ . In contrast, the Majorana mass for $\tilde{\Psi}_R$ is already present at tree level, arising from its coupling to σ . Nevertheless, due to the nontrivial \mathbb{Z}_4 charge of $\tilde{\Psi}_R$, this contribution does not participate neither in the linear nor in the inverse seesaw mechanisms. The field $\tilde{\Psi}_R$ is required instead to ensure anomaly cancellation of the $U(1)'$ gauge symmetry.

Finally, as will be shown later, the scalar fields σ and ρ are necessary to close the scalar line of the internal loop in Fig. 1 through the quartic interaction $\lambda_{\xi\sigma\chi\rho} (\xi \sigma^* \chi \rho + \text{h.c.})$, while the external loop is completed by the trilinear interaction $(A_{\phi\eta\varphi} \phi \eta \varphi + \text{h.c.})$.

Beyond its particle-physics implications, the spontaneous breaking of the discrete \mathbb{Z}_4 symmetry leads to the formation of cosmological domain walls (DWs) [92–94]. If persistent, these structures could eventually dominate the energy budget of the universe, disrupting primordial nucleosynthesis (BBN). A common resolution to this problem, assuming DWs form after inflation, is to introduce a small soft breaking parameter (e.g. $A_{\rho\rho^2}$) that renders them unstable (see e.g. Ref. [95] for other approaches). In this context, the soft-breaking mass terms provide a bias potential ΔV_{bias} that lifts the degeneracy between distinct vacua. This creates a pressure differential across the DWs, prompting their collapse once the breaking is sufficiently large [95–101]. The resulting decay rate is proportional to the magnitude of the soft-breaking parameters, while the DW lifetime τ_{DW} is inversely proportional. To ensure decay occurs before BBN and before DWs dominate the universe

($\tau_{\text{DW}} \lesssim t_{\text{DW}} \sim M_{\text{P}}^2/\sigma_\omega$), the bias must be large enough to satisfy $\tau_{\text{DW}} \approx \sigma_\omega/\Delta V_{\text{bias}} \lesssim 0.1$ s, where the wall tension is $\sigma_\omega \sim v_\rho^3$.

For a bias potential of the form $\Delta V_{\text{bias}} = \mu_{\text{bias}}^3 v_\rho$, these constraints translate into a lower bound on the symmetry-breaking scale [102]:

$$\frac{A_\rho}{\text{TeV}} \gtrsim \max \left[10^{-5} \left(\frac{v_\rho}{\text{TeV}} \right)^{2/3}, 10^{-5} \left(\frac{v_\rho}{\text{TeV}} \right)^{5/3} \right]. \quad (2.4)$$

This lower bound is sufficiently small, implying that including soft-breaking parameters would lead to subleading contributions to neutrino mass generation compared to the two-loop inverse and linear seesaw mechanisms considered here; therefore, they are neglected in this work.

The collapse of the DW network can generate a stochastic gravitational wave background, potentially observable by current and future experiments [101, 103]. A precise determination of the wall tension and bias potential requires a sophisticated analysis of the model's finite-temperature effective potential, as undertaken in works like [104–106]. Such a detailed study is reserved for future publication.

2.2 The scalar potential

The most general scalar potential invariant under the symmetries of the model, is given by:

$$\begin{aligned} V = & -\mu_\phi^2(\phi^\dagger\phi) - \mu_\sigma^2(\sigma^*\sigma) - \mu_\rho^2\rho^2 + \mu_\eta^2(\eta^\dagger\eta) + \mu_\varphi^2(\varphi^*\varphi) + \mu_\xi^2(\xi^*\xi) + \mu_\chi^2(\chi^*\chi) \\ & + (A_{\phi\eta\varphi}\phi\eta\varphi + \text{h.c.}) + \lambda_\phi(\phi^\dagger\phi)^2 + \lambda_\sigma(\sigma^*\sigma)^2 + \lambda_\rho\rho^4 + \lambda_\eta(\eta^\dagger\eta)^2 + \lambda_\varphi(\varphi^*\varphi)^2 \\ & + \lambda_\xi(\xi^*\xi)^2 + \lambda_\chi(\chi^*\chi)^2 + \lambda_{\phi\sigma}(\phi^\dagger\phi)(\sigma^*\sigma) + \lambda_{\phi\rho}(\phi^\dagger\phi)\rho^2 + \lambda_{\rho\sigma}\rho^2(\sigma^*\sigma) + \lambda_{\eta\varphi}(\eta^\dagger\eta)(\varphi^*\varphi) \\ & + \lambda_{\eta\xi}(\eta^\dagger\eta)(\xi^*\xi) + \lambda_{\eta\chi}(\eta^\dagger\eta)(\chi^*\chi) + \lambda_{\varphi\xi}(\varphi^*\varphi)(\xi^*\xi) + \lambda_{\varphi\chi}(\varphi^*\varphi)(\chi^*\chi) + \lambda_{\xi\chi}(\xi^*\xi)(\chi^*\chi) \\ & + \lambda_{\phi\eta}(\phi^\dagger\phi)(\eta^\dagger\eta) + \lambda'_{\phi\eta}(\phi\eta)(\eta^\dagger\phi^\dagger) + \lambda_{\phi\varphi}(\phi^\dagger\phi)(\varphi^*\varphi) + \lambda_{\phi\xi}(\phi^\dagger\phi)(\xi^*\xi) + \lambda_{\phi\chi}(\phi^\dagger\phi)(\chi^*\chi) \\ & + \lambda_{\sigma\eta}(\sigma^*\sigma)(\eta^\dagger\eta) + \lambda_{\sigma\varphi}(\sigma^*\sigma)(\varphi^*\varphi) + \lambda_{\sigma\xi}(\sigma^*\sigma)(\xi^*\xi) + \lambda_{\sigma\chi}(\sigma^*\sigma)(\chi^*\chi) \\ & + \lambda_{\rho\eta}\rho^2(\eta^\dagger\eta) + \lambda_{\rho\varphi}\rho^2(\varphi^*\varphi) + \lambda_{\rho\xi}\rho^2(\xi^*\xi) + \lambda_{\rho\chi}\rho^2(\chi^*\chi) + (\lambda_{\xi\sigma\chi\rho}\xi\sigma^*\chi\rho + \text{h.c.}). \quad (2.5) \end{aligned}$$

Observe that the ρ field can be assumed real without loss of generality.

We are interested in a scenario where the fields ϕ , σ , and ρ develop VEVs (v_ϕ , v_σ , and v_ρ , respectively), while the fields η , φ , ξ , and χ do not acquire any VEV, since the latter have non trivial charges under the preserved $\tilde{\mathbb{Z}}_2 \otimes \mathbb{Z}_3$ symmetry. Thus, in the scalar potential, we take $-\mu_\phi^2$, $-\mu_\sigma^2$, and $-\mu_\rho^2$ as negative, whereas μ_η^2 , μ_φ^2 , μ_ξ^2 and μ_χ^2 are taken to be positive. We adopt a CP-conserving scenario, which forbids mixing between CP-even and CP-odd scalars. This, in turn, implies that the trilinear coupling $A_{\phi\eta\varphi}$ and all quartic terms are real. Further restrictions on the parameters arise from potential stability and unitarity, detailed in Appendix B. The scalar fields are defined as follows:

$$\begin{aligned}
\phi &= \begin{pmatrix} \phi^+ \\ \frac{1}{\sqrt{2}}(v_\phi + h + i\phi_Z) \end{pmatrix}, & \eta &= \begin{pmatrix} \frac{1}{\sqrt{2}}(\eta_R^0 + i\eta_I^0) \\ \eta^- \end{pmatrix}, \\
\sigma &= \frac{1}{\sqrt{2}}(v_\sigma + \tilde{\sigma} + i\sigma_{Z'}), & \varphi &= \frac{1}{\sqrt{2}}\varphi_R + i\frac{1}{\sqrt{2}}\varphi_I, \\
\chi &= \frac{1}{\sqrt{2}}\chi_R + i\frac{1}{\sqrt{2}}\chi_I, & \xi &= \frac{1}{\sqrt{2}}\xi_R + i\frac{1}{\sqrt{2}}\xi_I. \\
\rho &= v_\rho + \tilde{\rho}, & &
\end{aligned} \tag{2.6}$$

where v_ϕ , v_σ , and v_ρ denote the VEVs responsible for breaking the electroweak symmetry, $U(1)'$, and \mathbb{Z}_4 , respectively. The scalar remnants of spontaneous symmetry breaking are h , $\tilde{\sigma}$, $\tilde{\rho}$, η^0 , η^- , φ , ξ , and χ . Moreover, ϕ^\pm , ϕ_Z , and $\sigma_{Z'}$ are the Goldstone bosons corresponding to the longitudinal components of the gauge fields W^\pm , Z , and Z' , respectively. Minimizing the scalar potential by setting its derivatives with respect to the VEVs to zero yields the following conditions on the couplings defined in Eq. (2.5):

$$2\lambda_\phi v_\phi^2 + \lambda_{\phi\sigma} v_\sigma^2 + 2\lambda_{\phi\rho} v_\rho^2 + 2\mu_\phi^2 = 0, \tag{2.7}$$

$$\lambda_{\phi\sigma} v_\phi^2 + 2\lambda_{\rho\sigma} v_\rho^2 + 2\lambda_\sigma v_\sigma^2 + 2\mu_\sigma^2 = 0, \tag{2.8}$$

$$\lambda_{\phi\rho} v_\phi^2 + \lambda_{\rho\sigma} v_\sigma^2 + 4\lambda_\rho v_\rho^2 + 2\mu_\rho^2 = 0. \tag{2.9}$$

After SSB there would be mixing among the scalars determined by the charges under \mathbb{Z}_3 which remains unbroken and the remnant $\tilde{\mathbb{Z}}_2$, dividing the scalars into three sectors, as follows: $(h, \tilde{\sigma}, \tilde{\rho})$, (η^0, χ) , and (ξ, φ) . Starting with the $\tilde{\mathbb{Z}}_2$ -even and \mathbb{Z}_3 neutral we have:

$$-\mathcal{L}_{\text{mass}}^{\tilde{\mathbb{Z}}_2\text{-even}, \mathbb{Z}_3\text{-neutral}} = \frac{1}{2} \begin{pmatrix} h & \tilde{\sigma} & \tilde{\rho} \end{pmatrix} \begin{pmatrix} 2\lambda_\phi v_\phi^2 & \lambda_{\phi\sigma} v_\phi v_\sigma & 2\lambda_{\phi\rho} v_\phi v_\rho \\ \lambda_{\phi\sigma} v_\phi v_\sigma & 2\lambda_\sigma v_\sigma^2 & 2\lambda_{\rho\sigma} v_\sigma v_\rho \\ 2\lambda_{\phi\rho} v_\phi v_\rho & 2\lambda_{\rho\sigma} v_\sigma v_\rho & 8\lambda_\rho v_\rho^2 \end{pmatrix} \begin{pmatrix} h \\ \tilde{\sigma} \\ \tilde{\rho} \end{pmatrix}. \tag{2.10}$$

The quartic couplings $\lambda_{\phi\sigma}$ and $\lambda_{\phi\rho}$ govern the extent of mixing between h and the additional scalars $\tilde{\sigma}$ and $\tilde{\rho}$, influencing deviations from the SM Higgs boson properties, which are tightly constrained by LHC Higgs measurements [107–109]. To align with these observations, we consider the alignment limit where $\lambda_{\phi\sigma} = \lambda_{\phi\rho} = 0$, ensuring h closely mimics the SM Higgs. In this scenario, the masses of the eigenstates $\tilde{\sigma}'$ and $\tilde{\rho}'$ can be analytically determined, with the mixing defined as:

$$\begin{pmatrix} \tilde{\sigma}' \\ \tilde{\rho}' \end{pmatrix} = \begin{pmatrix} \cos\theta & -\sin\theta \\ \sin\theta & \cos\theta \end{pmatrix} \begin{pmatrix} \tilde{\sigma} \\ \tilde{\rho} \end{pmatrix}, \tag{2.11}$$

where the mass eigenvalues and mixing angle are given by:

$$m_{\tilde{\sigma}'}^2 = 2\lambda_\sigma v_\sigma^2 + 8\lambda_\rho v_\rho^2 + \sqrt{(2\lambda_\sigma v_\sigma^2 - 8\lambda_\rho v_\rho^2)^2 + 4(2\lambda_{\rho\sigma} v_\rho v_\sigma)^2}, \quad (2.12)$$

$$m_{\tilde{\rho}'}^2 = 2\lambda_\sigma v_\sigma^2 + 8\lambda_\rho v_\rho^2 - \sqrt{(2\lambda_\sigma v_\sigma^2 - 8\lambda_\rho v_\rho^2)^2 + 4(2\lambda_{\rho\sigma} v_\rho v_\sigma)^2}, \quad (2.13)$$

$$\tan 2\theta = \frac{4\lambda_{\rho\sigma} v_\rho v_\sigma}{2\lambda_\sigma v_\sigma^2 - 8\lambda_\rho v_\rho^2}. \quad (2.14)$$

For the $\tilde{\mathbb{Z}}_2$ -even scalars charged under \mathbb{Z}_3 , the potential induces mixing among the scalar fields for both the imaginary and the real parts. The mass matrices for both real and imaginary components are presented compactly, differing only by the sign of the trilinear terms:

$$-\mathcal{L}_{\text{mass}}^{\tilde{\mathbb{Z}}_2\text{-even, } \mathbb{Z}_3\text{-charged}} = \frac{1}{2}(\eta_{R/I}, \varphi_{R/I}) \begin{pmatrix} \mu_\eta^2 + \frac{1}{2}\lambda_{\phi\eta}v_\phi^2 + \frac{1}{2}\lambda_{\sigma\eta}v_\sigma^2 + \lambda_{\rho\eta}v_\rho^2 & \pm \frac{1}{\sqrt{2}}A_{\phi\eta\varphi}v_\phi \\ \pm \frac{1}{\sqrt{2}}A_{\phi\eta\varphi}v_\phi & \mu_\varphi^2 + \frac{1}{2}\lambda_{\phi\varphi}v_\phi^2 + \frac{1}{2}\lambda_{\sigma\varphi}v_\sigma^2 + \lambda_{\rho\varphi}v_\rho^2 \end{pmatrix} \begin{pmatrix} \eta_{R/I} \\ \varphi_{R/I} \end{pmatrix}, \quad (2.15)$$

where + applies to the real parts (η_R, φ_R) and – to imaginary ones (η_I, φ_I) . Diagonalization proceeds via the following rotation:

$$\begin{pmatrix} \eta_{R/I} \\ \varphi_{R/I} \end{pmatrix} = R_{S_{R/I}} \begin{pmatrix} S_{1R/I} \\ S_{2R/I} \end{pmatrix} \quad \text{with} \quad R_{S_{R/I}} = \begin{pmatrix} \cos \theta_{S_{R/I}} & \sin \theta_{S_{R/I}} \\ -\sin \theta_{S_{R/I}} & \cos \theta_{S_{R/I}} \end{pmatrix}, \quad (2.16)$$

with the mixing angle given by:

$$\tan 2\theta_{S_{R/I}} = \frac{\pm\sqrt{2}A_{\phi\eta\varphi}v_\phi}{\left(\mu_\eta^2 + \frac{1}{2}\lambda_{\phi\eta}v_\phi^2 + \frac{1}{2}\lambda_{\sigma\eta}v_\sigma^2 + \lambda_{\rho\eta}v_\rho^2\right) - \left(\mu_\varphi^2 + \frac{1}{2}\lambda_{\phi\varphi}v_\phi^2 + \frac{1}{2}\lambda_{\sigma\varphi}v_\sigma^2 + \lambda_{\rho\varphi}v_\rho^2\right)}, \quad (2.17)$$

and the eigenvalues as below:

$$m_{S_{1R/I}}^2 = \frac{1}{2} \left[m_\eta^2 + m_\varphi^2 + \sqrt{(m_\eta^2 - m_\varphi^2)^2 + 2A_{\phi\eta\varphi}^2 v_\phi^2} \right], \quad (2.18)$$

$$m_{S_{2R/I}}^2 = \frac{1}{2} \left[m_\eta^2 + m_\varphi^2 - \sqrt{(m_\eta^2 - m_\varphi^2)^2 + 2A_{\phi\eta\varphi}^2 v_\phi^2} \right], \quad (2.19)$$

where $m_\eta^2 \equiv \mu_\eta^2 + \frac{1}{2}\lambda_{\phi\eta}v_\phi^2 + \frac{1}{2}\lambda_{\sigma\eta}v_\sigma^2 + \lambda_{\rho\eta}v_\rho^2$, $m_\varphi^2 \equiv \mu_\varphi^2 + \frac{1}{2}\lambda_{\phi\varphi}v_\phi^2 + \frac{1}{2}\lambda_{\sigma\varphi}v_\sigma^2 + \lambda_{\rho\varphi}v_\rho^2$. Note that trilinear terms enter only off-diagonally and with opposite sign for real and imaginary components, this makes the masses degenerate and the mixing angle having opposite sign ($\theta_{S_R} = -\theta_{S_I}$).

Similarly for the $\tilde{\mathbb{Z}}_2$ -odd scalars charged under \mathbb{Z}_3 , the mixing reads:

$$\mathcal{L}_{\text{mass}}^{\tilde{\mathbb{Z}}_2\text{-odd, } \mathbb{Z}_3\text{-charged}} = \frac{1}{2}(\xi_{R/I}, \chi_{R/I}) \begin{pmatrix} \mu_\xi^2 + \frac{1}{2}\lambda_{\phi\xi}v_\phi^2 + \frac{1}{2}\lambda_{\sigma\xi}v_\sigma^2 + \lambda_{\rho\xi}v_\rho^2 & \pm\lambda_{\xi\sigma\chi\rho}v_\rho v_\sigma \\ \pm\lambda_{\xi\sigma\chi\rho}v_\rho v_\sigma & \mu_\chi^2 + \frac{1}{2}\lambda_{\phi\chi}v_\phi^2 + \frac{1}{2}\lambda_{\sigma\chi}v_\sigma^2 + \lambda_{\rho\chi}v_\rho^2 \end{pmatrix} \begin{pmatrix} \xi_{R/I} \\ \chi_{R/I} \end{pmatrix}, \quad (2.20)$$

diagonalized by:

$$\begin{pmatrix} \xi_{R/I} \\ \chi_{R/I} \end{pmatrix} = \tilde{R}_{S_{R/I}} \begin{pmatrix} S_{3R/I} \\ S_{4R/I} \end{pmatrix} \quad \text{with} \quad \tilde{R}_{S_{R/I}} = \begin{pmatrix} \cos \gamma_{S_{R/I}} & \sin \gamma_{S_{R/I}} \\ -\sin \gamma_{S_{R/I}} & \cos \gamma_{S_{R/I}} \end{pmatrix}. \quad (2.21)$$

with mixing:

$$\tan 2\gamma_{S_{R/I}} = \frac{\pm 2\lambda_{\xi\sigma\chi\rho}v_\rho v_\sigma}{\left(\mu_\xi^2 + \frac{1}{2}\lambda_{\phi\xi}v_\phi^2 + \frac{1}{2}\lambda_{\sigma\xi}v_\sigma^2 + \lambda_{\rho\xi}v_\rho^2\right) - \left(\mu_\chi^2 + \frac{1}{2}\lambda_{\phi\chi}v_\phi^2 + \frac{1}{2}\lambda_{\sigma\chi}v_\sigma^2 + \lambda_{\rho\chi}v_\rho^2\right)}, \quad (2.22)$$

and eigenvalues:

$$m_{S_{3R/I}}^2 = \frac{1}{2} \left[m_\xi^2 + m_\chi^2 + \sqrt{(m_\xi^2 - m_\chi^2)^2 + 4\lambda_{\xi\sigma\chi\rho}v_\rho^2 v_\sigma^2} \right], \quad (2.23)$$

$$m_{S_{4R/I}}^2 = \frac{1}{2} \left[m_\xi^2 + m_\chi^2 - \sqrt{(m_\xi^2 - m_\chi^2)^2 + 4\lambda_{\xi\sigma\chi\rho}v_\rho^2 v_\sigma^2} \right], \quad (2.24)$$

where $m_\xi^2 \equiv \mu_\xi^2 + \frac{1}{2}\lambda_{\phi\xi}v_\phi^2 + \frac{1}{2}\lambda_{\sigma\xi}v_\sigma^2 + \lambda_{\rho\xi}v_\rho^2$, $m_\chi^2 \equiv \mu_\chi^2 + \frac{1}{2}\lambda_{\phi\chi}v_\phi^2 + \frac{1}{2}\lambda_{\sigma\chi}v_\sigma^2 + \lambda_{\rho\chi}v_\rho^2$. As before the masses will be degenerate between imaginary and real components and the mixing angle will have opposite sign ($\gamma_{S_R} = -\gamma_{S_I}$).

Lastly, the charged scalar η^- does not mix and its mass is given by:

$$m_\eta^2 = \mu_\eta^2 + \frac{1}{2}\lambda_{\phi\eta}v_\phi^2 + \frac{1}{2}\lambda_{\sigma\eta}v_\sigma^2 + \lambda_{\rho\eta}v_\rho^2. \quad (2.25)$$

2.3 Anomaly, stability and unitarity conditions

With the field content and interactions described in Section 2.1, we have verified that our model is anomaly free and checked the cancellation of both gauge and gravitational anomalies; the related conditions are listed in Appendix A. We recall that regarding the scalar potential, we choose $-\mu_\phi^2$, $-\mu_\sigma^2$, and $-\mu_\rho^2$ as negative and a CP-conserving scenario: with the trilinear coupling $A_{\phi\eta\varphi}$ and all quartic terms to be real. The other restrictions we impose on the parameters are due to potential stability and unitarity conditions that are detailed in Appendix B.

3 Neutrino mass generation

In this section we will explain the generation of the tiny active neutrino masses via an interplay of linear and inverse seesaw mechanisms ([110, 111]), here both dynamically generated at two loop level. With the particle content and symmetries shown in Table 1, we display the following complete neutrino Yukawa Lagrangian:

$$\begin{aligned} -\mathcal{L}_Y^{(\nu)} &= \sum_{i=1}^3 (y_\nu)_i \bar{l}_{iL} \tilde{\phi} \nu_R + M_N \bar{\nu}_R N_R^C + \sum_{i=1}^3 (y_\Psi)_{i1} \bar{l}_{iL} \eta \Psi_R + y_N \bar{\Psi}_L \varphi N_R \\ &+ y_\Omega \bar{\Omega}_L \xi \Psi_R + (z_\Psi)_1 N_R \varphi^* \bar{\Psi}_R^C + m_\Omega \bar{\Omega}_L \Omega_R \\ &+ (z_\Psi)_2 \sigma \bar{\Psi}_R^C \tilde{\Psi}_R + z_\Omega \bar{\Psi}_L \chi \Omega_R + \text{h.c.} \end{aligned} \quad (3.1)$$

In Section 2.2, we have already discussed how the scalar fields acquire their masses. In the remainder of this section, we analyze the corresponding case for neutral leptons—namely, the neutrino and Ψ field sectors—while the Ω fields already obtain their masses at tree level, as can be directly inferred from Eq. (3.1).

3.1 Generation of the LISS mechanism

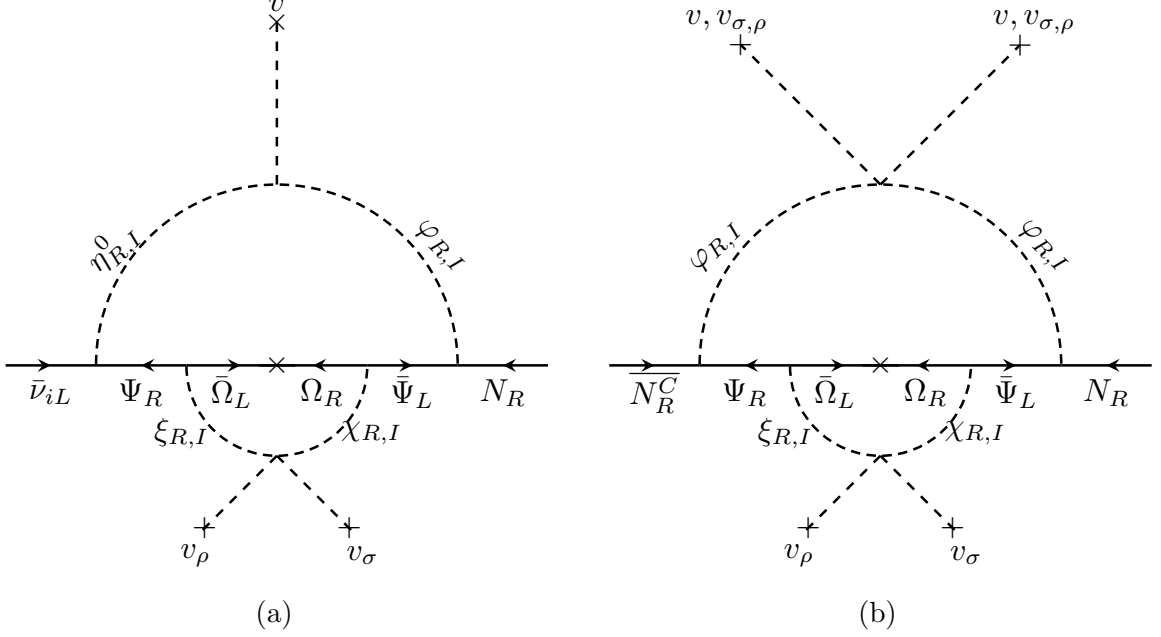


Figure 1: Two-loop diagrams for the neutrino mass submatrix ε (a) and for the lepton number violating Majorana mass term μ (b).

The neutrino Yukawa interactions of Eq. (3.1) induce the following neutrino mass terms:

$$\begin{aligned}
 -\mathcal{L}_{\text{mass}}^{(\nu)} &= \frac{1}{2} \left(\bar{\nu}_L^C \quad \bar{\nu}_R \quad \bar{N}_R \right) M_\nu \begin{pmatrix} \nu_L \\ \nu_R^C \\ N_R^C \end{pmatrix} + \text{h.c.} \\
 &= m_D \bar{\nu}_L \nu_R + \varepsilon \bar{\nu}_L N_R + M \bar{\nu}_R^C N_R + \frac{1}{2} \mu \bar{N}_R^C N_R + \text{h.c.}, \quad (3.2)
 \end{aligned}$$

where $m_{Di} \equiv (y_\nu)_i \frac{v}{\sqrt{2}}$ ($i = 1, 2, 3$) is the Dirac mass column vector. With this model, the tiny active neutrino masses are produced by a combination of linear and inverse seesaw mechanisms, where the full neutrino mass matrix expressed in the basis (ν_L, ν_R^C, N_R^C) , obtains the following structure:

$$M_\nu = \begin{pmatrix} 0 & m_D & \varepsilon \\ m_D^T & 0 & M \\ \varepsilon^T & M & \mu \end{pmatrix}, \quad (3.3)$$

where ν_{L_i} ($i = 1, 2, 3$) are the active neutrinos, whereas ν_R and N_R are the sterile ones,

Their lepton numbers are $L(\nu_L) = L(\nu_R) = -L(N_R) = 1$. Consequently, the sources of lepton number violation are the ε column vector and the μ entry. For the linear and inverse seesaw mechanisms to work appropriately, thus assuming the seesaw condition, the entries of the full neutrino mass matrix (3.3) must satisfy the following hierarchies: $\mu, \varepsilon_i \ll m_{D_i} \ll M$ (for $i = 1, 2, 3$). Furthermore, the column vector m_D and the entry M arise at tree level, whereas the column vector ε and the entry μ are generated at two-loop level as indicated in the Feynman diagrams (a) and (b) of Figure 1, respectively and they are given by:

$$m_{D_i} = (y_\nu)_i \frac{v}{\sqrt{2}}, \quad i = 1, 2, 3, \quad (3.4)$$

$$\begin{aligned} \varepsilon_i = & \sum_{s=1}^2 \sum_{p=1}^2 \frac{(y_\Psi)_{i1} y_\Omega y_N z_\Omega m_\Omega}{4(4\pi)^4} \\ & \times \int_0^1 d\alpha \int_0^{1-\alpha} d\beta \frac{1}{\alpha(1-\alpha)} \left[(R_{S_R})_{1s} (R_{S_R})_{2s} (\tilde{R}_{S_R})_{1p} (\tilde{R}_{S_R})_{2p} I(m_{\Omega_k}^2, m_{R_s R_{(p+2)}}^2, m_{R_s I_{(p+2)}}^2) \right. \\ & \left. + (R_{S_I})_{1s} (R_{S_I})_{2s} (\tilde{R}_{S_I})_{1p} (\tilde{R}_{S_I})_{2p} I(m_{\Omega_k}^2, m_{I_s R_{(p+2)}}^2, m_{I_s I_{(p+2)}}^2) \right], \quad i = 1, 2, 3, \quad (3.5) \end{aligned}$$

$$\begin{aligned} \mu = & \sum_{s=1}^2 \sum_{p=1}^2 \frac{(z_\Psi)_1 y_\Omega z_\Omega y_N m_\Omega}{4(4\pi)^4} \\ & \times \int_0^1 d\alpha \int_0^{1-\alpha} d\beta \frac{1}{\alpha(1-\alpha)} \left[(R_{S_R})_{2s} (R_{S_R})_{2s} (\tilde{R}_{S_R})_{1p} (\tilde{R}_{S_R})_{2p} I(m_{\Omega_k}^2, m_{R_s R_{(p+2)}}^2, m_{R_s I_{(p+2)}}^2) \right. \\ & \left. - (R_{S_I})_{2s} (R_{S_I})_{2s} (\tilde{R}_{S_I})_{1p} (\tilde{R}_{S_I})_{2p} I(m_{\Omega_k}^2, m_{I_s R_{(p+2)}}^2, m_{I_s I_{(p+2)}}^2) \right]. \quad (3.6) \end{aligned}$$

The two-loop integral entering in Eqs. (3.5) and (3.6) takes the form [37, 112]:

$$\begin{aligned} I(m_1^2, m_2^2, m_3^2) = & \frac{m_1^2 m_2^2 \ln\left(\frac{m_2^2}{m_1^2}\right) + m_2^2 m_3^2 \ln\left(\frac{m_3^2}{m_2^2}\right) + m_3^2 m_1^2 \ln\left(\frac{m_1^2}{m_3^2}\right)}{(m_1^2 - m_2^2)(m_1^2 - m_3^2)}, \\ m_{a_k b_l}^2 = & \frac{\beta m_{(S_k)_a}^2 + \alpha m_{(S_l)_b}^2}{\alpha(1-\alpha)}, \quad k, l = 1, 2, \quad a, b \in \{R, I\}. \quad (3.7) \end{aligned}$$

Finally, $R_{S_{R/I}}$ and $\tilde{R}_{S_{R/I}}$ in Eqs. (3.5) and (3.6) represent the rotation matrices that relate the interaction states to the physical CP-even and CP-odd scalar fields, as defined in Eqs. (2.16) and (2.21). Note that these four rotation matrices must fulfill the following orthogonality conditions:

$$\sum_{s=1}^2 (R_{S_a})_{1s} (R_{S_a})_{2s} = 0 \quad ; \quad \sum_{s=1}^2 (\tilde{R}_{S_a})_{1s} (\tilde{R}_{S_a})_{2s} = 0, \quad a \in \{R, I\}. \quad (3.8)$$

These conditions will be instrumental in understanding the discussion of the results presented in Section 5.

In the following, we proceed with the determination of the neutrino mass spectrum. Starting from the full neutrino mass matrix M_ν in Eq. (3.3), we first perform a perturbative block diagonalization under the seesaw conditions $\mu, m_D, \varepsilon \ll M$:

$$U'^T M_\nu U' \simeq \begin{pmatrix} \mathcal{M}_\nu^{\text{light}} & 0 \\ 0 & \mathcal{M}_H \end{pmatrix}, \quad (3.9)$$

where $\mathcal{M}_\nu^{\text{light}}$ is the 3×3 mass matrix of the light (active) neutrinos and \mathcal{M}_H is the 2×2 mass matrix of the heavy neutral fermions. This transformation is achieved through the matrix U' , which, in the seesaw limit, takes the form

$$U' \simeq \begin{pmatrix} 1 - \frac{1}{2} R R^\dagger & R \\ -R^\dagger & 1 - \frac{1}{2} R^\dagger R \end{pmatrix}, \quad \text{with} \quad R \equiv \begin{pmatrix} m_D & \varepsilon \end{pmatrix} \mathcal{M}_H^{-1}. \quad (3.10)$$

Explicitly, the matrix R is given by:

$$R = \begin{pmatrix} -\frac{\mu m_D + M \varepsilon}{M^2} & \frac{m_D}{M} \end{pmatrix}. \quad (3.11)$$

Due to the presence of the non-vanishing column LNV vector ε and the LNV Majorana mass parameter μ , small masses for the active neutrinos are generated within the scotogenic LISS framework. The light neutrinos thus acquire masses from the combined action of the linear [12, 13, 17] and inverse seesaw mechanisms [9–15], both dynamically generated in the present model. This yields the following light-neutrino mass matrix:

$$\mathcal{M}_\nu^{\text{light}} \simeq \frac{\mu}{M^2} m_D m_D^T - \frac{1}{M} (\varepsilon m_D^T + m_D \varepsilon^T), \quad (3.12)$$

whereas the heavy-sector mass matrix \mathcal{M}_H is approximately given by:

$$\mathcal{M}_H \simeq \begin{pmatrix} 0 & M \\ M & \mu \end{pmatrix}. \quad (3.13)$$

A final diagonalization step is performed on these two blocks. The light-neutrino mass matrix $\mathcal{M}_\nu^{\text{light}}$ is diagonalized by a unitary matrix R_ν , while \mathcal{M}_H is diagonalized by a unitary matrix R_M , yielding the physical neutrino masses. In this model, the light-neutrino sector contains one massless state, with the remaining two masses constrained by the solar and atmospheric mass-squared differences observed in oscillation experiments. The heavy neutrino mass spectrum, determined by \mathcal{M}_H and associated with the LNV parameter μ related to the inverse seesaw component of the full mass matrix M_ν in Eq. (3.3), consists of a pair of quasi-Dirac heavy neutrinos [113–115]. Their approximate masses are:

$$M_{N^-} \simeq -M + \frac{\mu}{2}, \quad (3.14)$$

$$M_{N^+} \simeq M + \frac{\mu}{2}. \quad (3.15)$$

Finally, the full neutrino mixing matrix U is then given by:

$$U \simeq \begin{pmatrix} (1 - \frac{1}{2} R R^\dagger) R_\nu & R R_M \\ -R^\dagger R_\nu & (1 - \frac{1}{2} R^\dagger R) R_M \end{pmatrix}. \quad (3.16)$$

3.2 Majorana mass generation for the dark neutral leptons Ψ_R and $\tilde{\Psi}_R$

The fermions Ψ_R and $\tilde{\Psi}_R$ behave differently under the symmetries of the model, which leads to qualitatively distinct origins for their Majorana masses. The $\tilde{\Psi}_R$ acquires a Majorana mass term from Eq. (3.1), after $U(1)'$ breaking given by: $\langle \sigma \rangle = v_\sigma / \sqrt{2}$,

$$m_{\tilde{\Psi}_R} = \frac{(z_\Psi)_2 v_\sigma}{\sqrt{2}}. \quad (3.17)$$

On the other hand, a Majorana mass for Ψ_R is forbidden at tree level by the \mathbb{Z}_3 symmetry, but arises radiatively at one loop through the internal loop of the diagrams of Fig 1. This Majorana mass is given by:

$$m_{\Psi_R} = \frac{z_\Omega y_\Omega m_\Omega}{8\pi^2} \sum_{p=1}^2 \left[(\tilde{R}_{S_R})_{2p} (\tilde{R}_{S_R})_{1p} \frac{m_{S_{(p+2)R}}^2}{m_{S_{(p+2)R}}^2 - m_\Omega^2} \ln \left(\frac{m_{S_{(p+2)R}}^2}{m_\Omega^2} \right) \right. \\ \left. - (\tilde{R}_{S_I})_{2p} (\tilde{R}_{S_I})_{1p} \frac{m_{S_{(p+2)I}}^2}{m_{S_{(p+2)I}}^2 - m_\Omega^2} \ln \left(\frac{m_{S_{(p+2)I}}^2}{m_\Omega^2} \right) \right]. \quad (3.18)$$

4 Phenomenology

Our model provides a rich phenomenology. In this section, we focus on laboratory probes: we briefly discuss how collider searches could test our framework and outline future directions to explore, while primarily concentrating on charged-lepton–flavor–violating (cLFV) observables and on the predictions for Muonium decays and Muonium–antimuonium oscillations. Cosmological aspects, such as dark-matter production and domain-wall dynamics, are left for future work.

4.1 Collider searches

Here we provide a concise qualitative discussion of the collider signatures of Dirac sterile neutrinos $\Omega_{L,R}$, heavy Z' , and dark matter candidates. The heavy quasi-Dirac sterile neutrinos can be produced at the LHC in association with a SM charged lepton via quark–antiquark annihilation, which corresponds to the Drell–Yan (DY) mechanism. Furthermore, like the $U(1)'$ scenario in Ref. [116], our model predicts two-body sterile neutrino decays $N \rightarrow l_i^\pm W^\mp$, $\nu_i Z$ and $\nu_i h$ (with flavor index $i = 1, 2, 3$), suppressed by the small active–sterile mixing angle $\theta \sim \mathcal{O}(10^{-3})$, which should be constrained to maintain charged LFV decays well below present experimental limits and remain consistent with unitarity requirements [117, 118]. These decays mediate three-body final states such as $N \rightarrow l_i^+ l_j^- \nu_k$, $N \rightarrow l_i^- u_j \bar{d}_k$, $N \rightarrow b \bar{b} \nu_k$ (where $i, j, k = 1, 2, 3$ are flavor indices), which are also present in Ref. [116]. Consequently, we expect that our total cross-section predictions for the LFV process $pp \rightarrow NN \rightarrow e^\pm \mu^\mp 4j$ and sterile neutrino lifetimes will align closely with those of

Ref. [116]. However, a slight deviation is expected in the decay rate of $N \rightarrow l_i^+ l_j^- \nu_k$, as our model includes contributions from off-shell W gauge bosons.

Regarding Z' production, it is worth noting that the Z' can be produced at proton–proton colliders through both the DY mechanism and Vector Boson Fusion (VBF). Once produced, the heavy Z' gauge boson can decay into fermion–antifermion pairs, leading to characteristic signatures with dilepton or dijet final states, such as $pp \rightarrow Z' \rightarrow l^+ l^-$, $pp \rightarrow Z' \rightarrow 2j$, $pp \rightarrow Z', 2j \rightarrow l^+ l^- 2j$, and $pp \rightarrow Z', 2j \rightarrow 4j$. Detailed studies of Z' production at colliders within $B - L$ gauge theories are presented in Ref. [36]. The constraint $\frac{M_{Z'}}{g_X} > 7$ TeV, derived from LEP I/II measurements of $e^+ e^- \rightarrow l^+ l^-$ [119–121], is further supported by LHC searches [122, 123]. Additional bounds on $\frac{M_{Z'}}{g_{B-L}}$ from LEP II and projected sensitivities at future $e^+ e^-$ colliders (e.g., ILC) are analyzed in Ref. [121].

On the other hand, thanks to the conserved $\tilde{\mathbb{Z}}_2$ and \mathbb{Z}_3 symmetries, the dark matter candidates are pair-produced. The neutral components of the inert doublet can be pair-produced through two primary mechanisms: DY processes mediated by the Z boson or VBF. At colliders, these production channels lead to a distinctive signature of two jets accompanied by missing transverse energy. The DY production channel of inert doublet pairs at the LHC is analyzed in [84]. In addition, for the VBF production channel specifically, comprehensive analyses of the resulting collider signatures are presented in Ref. [124]. Furthermore, as in the model of Ref. [84], in the fermionic dark matter scenario, the pair production of the charged inert doublet components via the Drell–Yan process, followed by their subsequent decays, can generate a distinctive opposite-sign dilepton plus missing transverse energy (MET) signature. An observed excess of such events above the Standard Model background predictions at the LHC would provide supporting evidence for this model. While a comprehensive analysis of these collider signatures represents an important future direction, it falls outside the scope of the current study.

Finally, the ratio $\frac{M_{Z'}}{g_X}$ can also be constrained from dark matter direct detection measurements on the upper limit of the spin-independent WIMP–nucleon cross section. In the fermionic dark matter scenario, Z' exchange leads to spin-independent scattering with nucleons, along similar lines to Ref. [41]. In the limit of small momentum transfer, the Z' exchange gives rise to a spin-independent scattering with nucleons. The corresponding cross section per nucleon takes the form [125]

$$\sigma \simeq \frac{g_X^4}{\pi} \frac{m_n^2 m_{\Psi_R}^2}{(m_n + m_{\Psi_R})^2 M_{Z'}^4}, \quad (4.1)$$

where m_n is the nucleon mass, and $f_n \sim 0.3$ is the hadron matrix element. Given that the mass for our fermionic dark matter candidate Ψ_R arises at one loop, we consider its mass to be around the 10 GeV scale, which implies that its spin independent cross section for direct detection should be smaller than $4.8 \times 10^{-47} \text{cm}^2$, as follows from the data provided by the

LUX experiment [91]. Consequently, the constraints arising from the LUX experiment [91] set the ratio $\frac{M_{Z'}}{g_X}$ to be larger than about 40 TeV for a 10 GeV fermionic dark matter mass.

4.2 Charged lepton flavor violation

Here we discuss the implications of our model in charged lepton flavor violating decays such as $\ell_\alpha \rightarrow \ell_\beta \ell_\beta \ell_\rho$, $\text{CR}(\mu - e, N)$, and the radiative ones, $\ell \rightarrow \ell' \gamma$.

In this model, the neutral spectrum is composed of seven heavy sterile neutrinos and among them, given the \mathbb{Z}_3 charge assignment only ν_R and ψ_{1R} provide contribution to the penguin and box diagrams of these cLFV observables. The scalar sector may also contribute and due to the symmetries, only the charged component of the scalar doublet η provides a contribution at one-loop level.

4.2.1 Radiative cLFV decays

As discussed above, the computation of the decay amplitude for radiative $l_i \rightarrow l_j \gamma$ ($\mu \rightarrow e \gamma$, $\tau \rightarrow \mu \gamma$ and $\tau \rightarrow e \gamma$) decays due to both the neutral fermions and the scalar field η contributions [43, 44, 82, 84, 126–134] leads to the following branching ratio:

$$\text{Br}(l_i \rightarrow l_j \gamma) = \left| \left(\frac{\alpha_W^3 s_W^2 m_{l_i}^5}{256 \pi^2 m_W^4 \Gamma_i} \right)^{1/2} G_{ij} + \left(\frac{3(4\pi)^3 \alpha_{EM}}{4G_F^2} \right)^{1/2} \sum_{k=1}^3 \frac{z_{kj}^* z_{ki}}{2(4\pi)^2 m_{\eta^\pm}^2} F_2(\xi) \right|^2, \quad (4.2)$$

$$G_{ij} \simeq \sum_{k=1}^3 \left(\left[\left(1 - \frac{1}{2} R R^\dagger \right) R_\nu \right]_{ik}^* \right) \left(\left(1 - \frac{1}{2} R R^\dagger \right) R_\nu \right)_{jk} G_\gamma \left(\frac{m_{\nu_k}^2}{m_W^2} \right) + 2 \sum_{k=1}^2 (R)_{ik}^* (R)_{jk} G_\gamma \left(\frac{m_{N_k}^2}{m_W^2} \right), \quad (4.3)$$

$$G_\gamma(x) \equiv \frac{10 - 43x + 78x^2 - 49x^3 + 18x^3 \ln x + 4x^4}{12(1-x)^4}, \quad (4.4)$$

$$F_2(x) = \frac{1 - 6x + 3x^2 + 2x^3 - 6x^2 \ln x}{6(1-x)^4}. \quad (4.5)$$

Here $z_{is} = \sum_{k=1}^3 y_{\Psi}^{ks} (V_{LL}^\dagger)_{ik}$, V_{LL} being the charged lepton mixing matrix in general, R and R_ν are defined in Section 3.1, s_W corresponds to the sine of the weak mixing angle and Γ_i is the total decay width of the charged lepton with its mass denoted by m_{l_i} . For simplicity, in our calculation we work in the charged-lepton mass basis, so that $(V_{LL}^\dagger)_{ik} = \delta_{ik}$ and z_{is} reduces to the Yukawa couplings y_{Ψ}^{is} .

The first term in Eq. (4.2) corresponds to the contribution of the neutral fermions, while the second one arises from the charged component of the dark scalar doublet η . The argument of the associated loop function is $\xi = \frac{m_{\Psi_R}^2}{m_{\eta^\pm}^2}$, which is given by the mass ratio of Ψ_R and η^\pm , as defined in (3.18) and (2.25), respectively.

4.2.2 CR($\mu - e, N$)

The $\mu - e$ conversion occurs in a muonic atom formed when a muon is captured, falling into the first state of a target nucleus N . The conversion rate is defined as

$$\text{CR}(\mu - e, N) \equiv \frac{\Gamma(\mu^- + N \rightarrow e^- + N)}{\Gamma(\mu^- + N \rightarrow \text{all})}. \quad (4.6)$$

The box and penguin diagrams inducing $\mu - e$ conversion receive both neutrino and scalar contributions which are given by:

$$\begin{aligned} \text{CR}(\mu - e, N) = & \left| \sqrt{\frac{2 G_F^2 \alpha_W^2 m_\mu^5}{(4\pi)^2 \Gamma_{\text{capt}}(Z)} \left[4 V^{(p)} \left(2 \tilde{F}_u^{\mu e} + \tilde{F}_d^{\mu e} \right) + 4 V^{(n)} \left(\tilde{F}_u^{\mu e} + 2 \tilde{F}_d^{\mu e} \right) + D G_\gamma^{\mu e} \frac{s_W^2}{2\sqrt{4\pi\alpha}} \right]} \right. \\ & + \left[\frac{p_e E_e m_\mu^3 G_F^2 \alpha_{\text{EM}}^3 Z_{\text{eff}}^4 F_p^2}{8\pi^2 Z \Gamma_{\text{capt}}} \left[\left| (Z + N) \left(g_{LS}^{(0)} \right) + (Z - N) \left(g_{LS}^{(1)} \right) \right|^2 \right. \right. \\ & \left. \left. + \left| (Z + N) \left(g_{RS}^{(0)} \right) + (Z - N) \left(g_{RS}^{(1)} \right) \right|^2 \right] \right]^{\frac{1}{2}} \Big|, \end{aligned} \quad (4.7)$$

where G_F is the Fermi constant, m_μ the muon mass, $\alpha_{\text{EM}} \equiv e^2/(4\pi)$, with s_W corresponding to the sine of the weak mixing angle and $\Gamma_{\text{capt}}(Z)$ denotes the capture rate of a nucleus with atomic number Z [135]. The form factors $\tilde{F}_q^{\mu e}$ ($q = u, d$) are given by

$$\tilde{F}_q^{\mu e} = Q_q s_W^2 F_\gamma^{\mu e} + F_Z^{\mu e} \left(\frac{I_q^3}{2} - Q_q s_W^2 \right) + \frac{1}{4} F_{\text{box}}^{\mu e q q}, \quad (4.8)$$

where Q_q denotes the quark electric charge ($Q_u = 2/3$, $Q_d = -1/3$) and I_q^3 is the weak isospin ($\mathcal{I}_u^3 = 1/2$, $\mathcal{I}_d^3 = -1/2$). The quantities $F_\gamma^{\mu e}$, $F_Z^{\mu e}$ and $F_{\text{box}}^{\mu e q q}$ correspond to the different form factors of the diagrams, and $G_\gamma^{\mu e}$ corresponds to the dipole term; all expressions are collected in Appendix C. The relevant information (nuclear form factors and averages over the atomic electric field) is encoded in the form factors F_p , D , $V^{(p)}$, and $V^{(n)}$. In our analysis, we use the numerical values presented in Ref. [135].

In the above, the effective nucleon couplings $g_{LS}^{(0)}$ and $g_{LS}^{(1)}$ can be expressed in terms of the quark-level scalar couplings as

$$\begin{aligned} g_{LS}^{(0)} &= \frac{1}{2} \sum_{q=u,d,s} \left(g_{LS}^{(q)} G_S^{(q,p)} + g_{LS}^{(q)} G_S^{(q,n)} \right), \\ g_{LS}^{(1)} &= \frac{1}{2} \sum_{q=u,d,s} \left(g_{LS}^{(q)} G_S^{(q,p)} - g_{LS}^{(q)} G_S^{(q,n)} \right). \end{aligned} \quad (4.9)$$

Only the light quark flavors u , d , and s provide sizable contributions. In Appendix D, we express the quark-level scalar couplings $g_{LS}^{(q)}$ in terms of the parameters of our model. The corresponding scalar form factors entering the nucleon matrix elements are taken from Refs. [136, 137].

$$\begin{aligned} G_S^{(u,p)} = G_S^{(d,n)} &= 5.1, & G_S^{(d,p)} = G_S^{(u,n)} &= 4.3, \\ G_S^{(s,p)} = G_S^{(s,n)} &= 2.5. \end{aligned} \quad (4.10)$$

4.2.3 $\ell_\alpha \rightarrow \ell_\beta \ell_\beta \ell_\rho$

The branching ratio for the three body charged lepton flavor violating decay $\ell_\beta \rightarrow \ell_\alpha \bar{\ell}_\alpha \ell_\alpha$ takes the form [131, 132, 138, 139]:

$$\begin{aligned} \text{BR}(\ell_\beta \rightarrow \ell_\alpha \bar{\ell}_\alpha \ell_\alpha) = & \left| \left[\frac{\alpha_W^4}{24576 \pi^3} \frac{m_\beta^4}{M_W^4} \frac{m_\beta}{\Gamma_\beta} \times \left\{ 2 \left| \frac{1}{2} F_{\text{box}}^{\beta 3\alpha} + F_Z^{\beta\alpha} - 2s_W^2 (F_Z^{\beta\alpha} - F_\gamma^{\beta\alpha}) \right|^2 \right. \right. \right. \\ & + 4s_W^4 |F_Z^{\beta\alpha} - F_\gamma^{\beta\alpha}|^2 + 16s_W^2 \text{Re} \left[(F_Z^{\beta\alpha} - \frac{1}{2} F_{\text{box}}^{\beta 3\alpha}) G_\gamma^{\beta\alpha*} \right] \\ & - 48s_W^4 \text{Re} \left[(F_Z^{\beta\alpha} - F_\gamma^{\beta\alpha}) G_\gamma^{\beta\alpha*} \right] + 32s_W^4 |G_\gamma^{\beta\alpha}|^2 \left[\log \frac{m_\beta^2}{m_\alpha^2} - \frac{11}{4} \right] \left. \right]^{\frac{1}{2}} \\ & + \left[\frac{3(4\pi)^2 \alpha_{\text{EM}}^2}{8 G_F^2} \left[|A_{ND}|^2 + |A_D|^2 \left(\frac{16}{3} \log \left(\frac{m_\beta}{m_\alpha} \right) - \frac{22}{3} \right) + \frac{1}{6} |B|^2 \right. \right. \\ & \left. \left. + \left(-2A_{ND} A_D^* + \frac{1}{3} A_{ND} B^* - \frac{2}{3} A_D B^* + \text{h.c.} \right) \right] \text{BR}(\ell_\beta \rightarrow \ell_\alpha \nu_\beta \bar{\nu}_\alpha) \right]^{\frac{1}{2}} \right|^2. \end{aligned} \quad (4.11)$$

The dipole form factor is given by

$$A_D = \sum_{i=1}^3 \frac{z_{i\beta}^* z_{i\alpha}}{2(4\pi)^2 m_{\eta^+}^2} F_2(\xi). \quad (4.12)$$

The form factor A_{ND} is generated from the non-dipole photon penguin diagrams and is expressed as

$$A_{ND} = \sum_{i=1}^3 \frac{z_{i\beta}^* z_{i\alpha}}{6(4\pi)^2 m_{\eta^+}^2} G_2(\xi). \quad (4.13)$$

In addition to that, the contribution of box diagrams generates the form factor B , which is given by

$$e^2 B = \frac{1}{(4\pi)^2 m_{\eta^+}^2} \sum_{i,j=1}^3 \left[\frac{1}{2} D_1(\xi_i, \xi_j) z_{j\beta}^* z_{j\beta} z_{i\beta}^* z_{i\alpha} + \sqrt{\xi_i \xi_j} D_2(\xi_i, \xi_j) z_{j\beta}^* z_{j\beta}^* z_{i\beta} z_{i\alpha} \right], \quad (4.14)$$

where the different loop functions take the form

$$G_2(x) = \frac{2 - 9x + 18x^2 - 11x^3 + 6x^3 \log x}{6(1-x)^4}, \quad (4.15)$$

$$D_1(x, y) = -\frac{1}{(1-x)(1-y)} - \frac{x^2 \log x}{(1-x)^2(x-y)} - \frac{y^2 \log y}{(1-y)^2(y-x)}, \quad (4.16)$$

$$D_2(x, y) = -\frac{1}{(1-x)(1-y)} - \frac{x \log x}{(1-x)^2(x-y)} - \frac{y \log y}{(1-y)^2(y-x)}. \quad (4.17)$$

and $F_2(x)$ was already defined in Eq. (4.5). The remaining form factors present in the neutrino contribution — also relevant for $\mu - e$ conversion — are collected in Appendix C.

4.3 Muonium decays and Muonium-antimuonium oscillation

Formed in matter when a μ^+ slows down and captures an e^- , Muonium (Mu) is a hydrogen-like bound state ($e^-\mu^+$) [140]. Being free from hadronic interactions and with its electromagnetic structure precisely predicted in the SM, Mu provides an excellent system for high-precision measurements of fundamental constants and for testing new physics. Moreover, its cLFV transitions are essentially free from nuclear uncertainties. In this work, we consider the contributions of our model to the cLFV decay $\text{Mu} \rightarrow e^+e^-$ [141] and to Muonium-antimuonium conversion [142].

The decay $\text{Mu} \rightarrow e^+e^-$ is strictly forbidden in the Standard Model. In some of its extensions with right-handed neutrinos, this decay has been studied both at low energies and in the context of a future muon collider [141]. The cLFV Muonium decay rate can be written as

$$\text{BR}(\text{Mu} \rightarrow e^+e^-) = \frac{\alpha_{\text{EM}}^3}{32\pi^2\Gamma_\mu} \frac{m_e^2 m_\mu^2}{(m_e + m_\mu)^3} \sqrt{1 - 4 \frac{m_e^2}{(m_e + m_\mu)^2}} |\mathcal{M}_{\text{tot}}|^2, \quad (4.18)$$

where the amplitude \mathcal{M}_{tot} receives contributions from penguin and box diagrams with heavy neutrinos and dark scalar exchange [141, 143]. The strongest limit to date, set by the PSI experiment [144], is

$$\text{BR}(\text{Mu} \rightarrow e^+e^-) < 5.7 \times 10^{-6}. \quad (4.19)$$

with the feasible future sensitivity lying around $\text{BR}(\text{Mu} \rightarrow e^+e^-) < 1 \times 10^{-12}$ [145].

While the decay $\text{Mu} \rightarrow e^+e^-$ probes cLFV through a short-distance annihilation process, Muonium-antimuonium oscillations test a qualitatively different regime. Instead of a decay within the bound state, the system undergoes a LFV transition into its antiparticle, $\overline{\text{Mu}} = e^+\mu^-$. This conversion is a striking signature of new physics [142]: its observation would constitute unambiguous evidence for $|\Delta L_{e,\mu}| = 2$ interactions and is sensitive to operators that are not necessarily the same as those contributing to the cLFV decay.

This transition can be described by the effective interaction for $e^-\mu^+ \rightarrow e^+\mu^-$, which for a $(V - A) \times (V - A)$ structure [137] reads

$$\mathcal{L}_{\text{eff}}^{\text{M}\overline{\text{M}}} = \frac{G_{\text{M}\overline{\text{M}}}}{\sqrt{2}} (\overline{\mu}\gamma^\alpha(1 - \gamma_5)e) (\overline{e}\gamma_\alpha(1 - \gamma_5)\mu), \quad (4.20)$$

where $G_{\text{M}\overline{\text{M}}}$ parametrizes the strength of the new interaction. It induces a small energy splitting between the Mu and $\overline{\text{Mu}}$ ground states,

$$\delta_E^{\text{M}-\overline{\text{M}}} = \frac{8G_F}{\sqrt{2}n^2\pi a_0^3} \left(\frac{G_{\text{M}\overline{\text{M}}}}{G_F} \right), \quad (4.21)$$

where n is the principal quantum number and a_0 the Bohr radius.

At present, no positive signal has been found; the best limit has been set at PSI [144], where Muonium atoms are formed by electron capture when positively charged muons (from a very intense muon beam) are stopped in a SiO₂ powder target and are given by [144]:

$$P(\text{Mu} \rightarrow \overline{\text{Mu}}) < 8.3 \times 10^{-11} \quad \Rightarrow \quad |G_{\text{MM}}| < 3.0 \times 10^{-3} G_F. \quad (4.22)$$

Future experiments such as MACE (CSNS) [146] and J-PARC [147] aim to reach $P(\text{Mu} \rightarrow \overline{\text{Mu}}) \sim 10^{-14}$.

5 Results

In this section, we present the numerical results of our model. We have performed a comprehensive scan over the parameter space defined in Sections 2 and 3, including neutrino Yukawa couplings, pseudo-Dirac masses, and charged scalar masses. For each parameter point, we impose consistency with the global fit to neutrino oscillation data from Ref. [148] at the 3σ level, as well as the stability and unitarity conditions derived in Appendix B. Throughout this section, we present results for both normal (NO) and inverted (IO) neutrino mass orderings and examine their implications for charged lepton flavor violation and muonium-related observables.

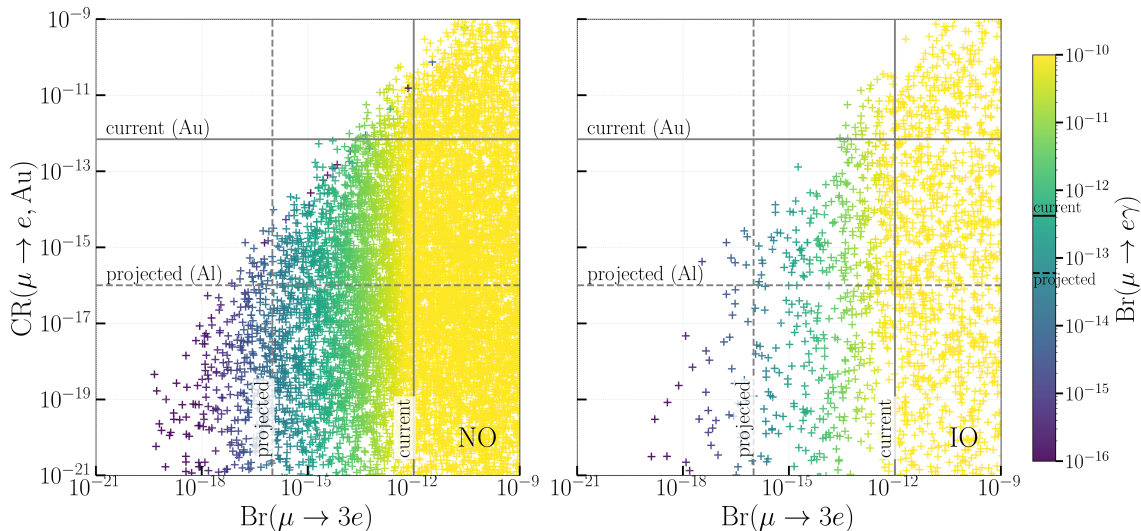


Figure 2: Correlation among cLFV observables. Points allowed by the model and consistent with neutrino oscillation data assuming normal (inverted) ordering are shown in the left (right) panel. Current bounds are indicated by solid lines, while future projections are shown as dashed lines.

We start with the most constraining cLFV observables in the muon sector. Figure 2 shows the correlation between the $\mu \rightarrow e$ conversion rate in gold and the $\mu \rightarrow eee$ branching

ratio for normal (left-panel) and inverted (right-panel) neutrino mass orderings. The color scale represents the corresponding $\mu \rightarrow e\gamma$ branching ratio. Our findings reveal a strong preference for the normal mass ordering over the inverted hierarchy, as it accommodates a vastly greater number of phenomenologically viable parameter points. There is also a clear trend where larger $\mu \rightarrow eee$ branching ratios imply larger $Br(\mu \rightarrow e\gamma)$. Out of the two contributions to cLFV, arising from the scalar and neutrino sectors, we have verified that the charged scalar mediators provide the dominant contribution due to the small mixings ($U_{\alpha 4}, U_{\alpha 5}$) required by neutrino data. Finally, it is also important to note that while the neutrino contributions to $\mu - e$ conversion and $\mu \rightarrow 3e$ are strongly correlated—since the same type of form factors contribute to both processes—this is no longer the case for the scalar contribution, which breaks the correlation.

After analyzing the cLFV observables in the muon sector, it is natural to ask whether other cLFV processes, such as τ decays, can also provide relevant constraints. To address this question, Figure 3 shows the most constraining branching ratios for τ -sector cLFV, namely $Br(\tau \rightarrow e\gamma)$ and $Br(\tau \rightarrow \mu\gamma)$. The figure displays the points allowed by neutrino data, as well as the stability and unitarity conditions, for both normal (NO, red) and inverted (IO, blue) neutrino mass orderings. Points shown in grey correspond to regions already excluded by cLFV constraints from the muon sector. We observe that, after applying these constraints, the surviving points lie close to the current experimental bounds from τ decays, with a few additional points further excluded. Therefore, while τ decays are not as restrictive as those in the muon sector, they still provide complementary sensitivity and are not completely negligible.

While scalar loops dominate the cLFV observables, the heavy neutrinos themselves are subject to direct search constraints. Figure 4 shows the active–sterile mixing, quantified by $|U_{\alpha 4}|^2 + |U_{\alpha 5}|^2$ (with $\alpha = e, \mu, \tau$), as a function of the heavy neutrino mass M_N . All points displayed are consistent with neutrino oscillation data, as well as stability and unitarity conditions. Points excluded by cLFV observables are shown in grey, while the grey shaded regions indicate the exclusion limits from current direct search experiments. It is worth emphasizing that, although many points are ruled out by cLFV bounds, those processes are dominated by the scalar contribution. Therefore, when projected onto the plane of neutrino mixings, the allowed regions for large active–sterile mixing remain essentially unaffected.

To further understand the neutrino mass generation mechanism in the model and the interplay between linear and inverse seesaw mechanisms, we show in Figure 5 the correlation between the inverse seesaw mass parameter μ and the linear seesaw parameter ε , where all points shown are consistent with neutrino oscillation experimental data. The red and blue points are compatible with charged lepton flavor violating constraints and correspond to

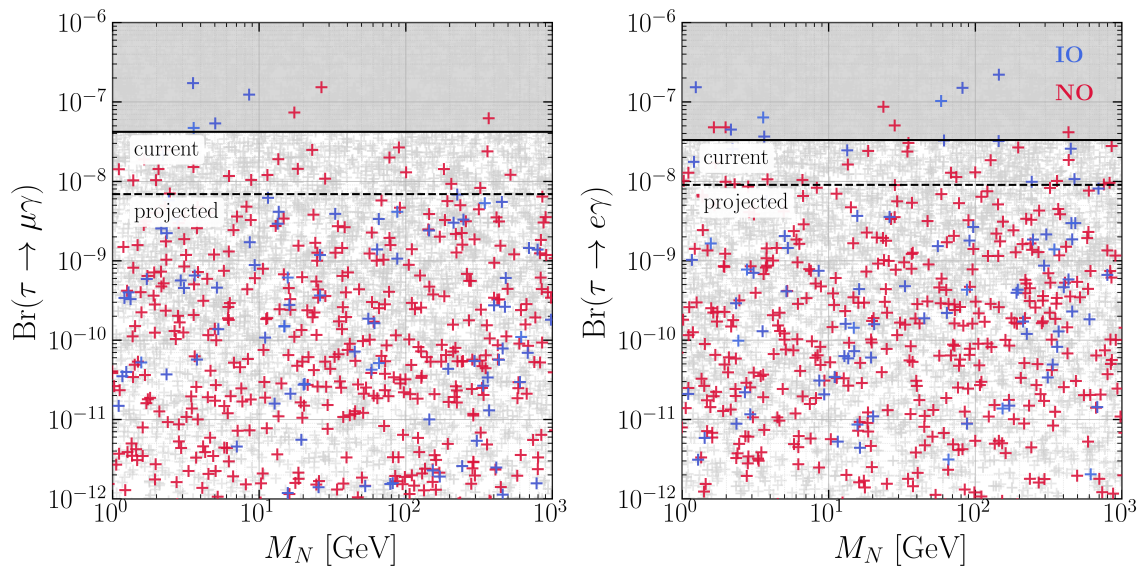


Figure 3: Most constraining cLFV τ decays are shown. In the left panel, we display $\text{Br}(\tau \rightarrow \mu\gamma)$ as a function of M_N , and in the right panel, the equivalent plot for $\text{Br}(\tau \rightarrow e\gamma)$. Red and blue crosses correspond to predictions consistent with normal (NO) and inverted (IO) neutrino mass orderings, respectively. Grey crosses indicate points excluded by other experimental constraints. The solid black lines denote the current experimental limits, while future projections are shown as dashed lines.

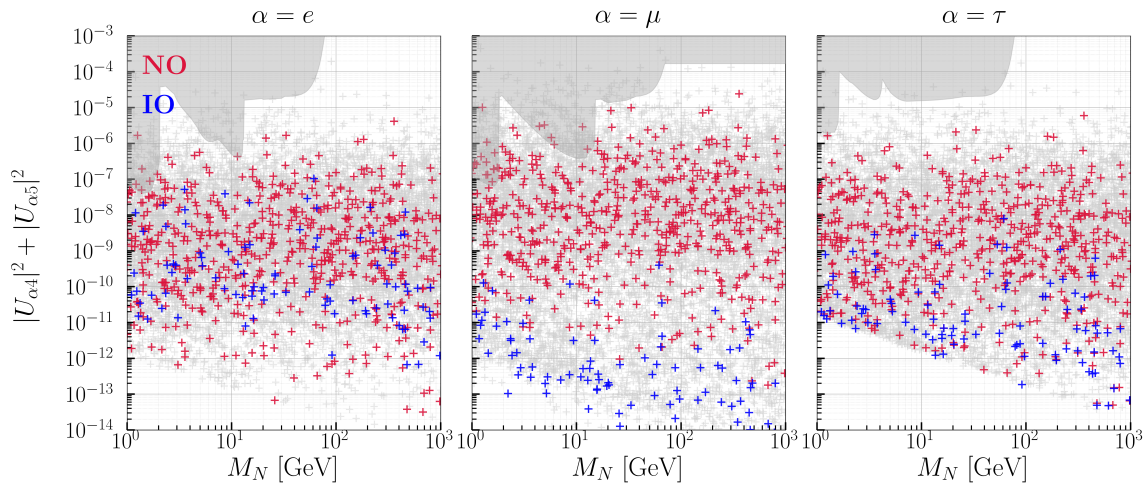


Figure 4: Points consistent with neutrino oscillation data and allowed by the model. Red (blue) points correspond to normal (inverted) mass ordering. The gray shaded regions denote current experimental constraints[149], while gray points are excluded by existing cLFV constraints.

the scenarios of normal and inverted neutrino mass orderings, respectively. We have found that the lepton number violating mass parameter μ is in general larger than the linear seesaw parameter ε . This suppression can be understood directly from the orthogonality conditions in Eq. (3.1) which provides partial cancellation for ε_i ($i = 1, 2, 3$) explaining its suppression. This slight preference for the inverse seesaw is consistent with the underlying mechanisms, as the inverse seesaw contribution scales quadratically with the $\frac{m_D}{M}$ ratio, while the linear seesaw scales linearly. This analysis shows that the atmospheric mass squared splitting is generated from the inverse seesaw mechanism, whereas the solar mass squared difference arises from the linear seesaw.

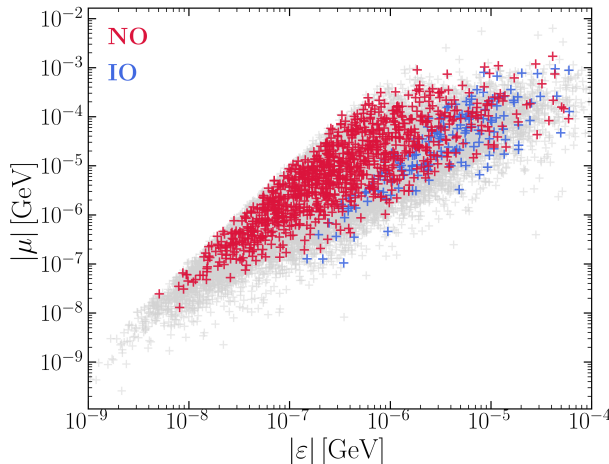


Figure 5: Correlation between the inverse seesaw parameter (μ) and the linear seesaw term (ε). Points consistent with neutrino oscillation data and allowed by the model are shown. Red (blue) points correspond to normal (inverted) mass ordering, while gray points are excluded by current cLFV constraints.

Finally, we comment on the model predictions for Muonium observables. The cLFV decay $\text{Mu} \rightarrow e^+e^-$ and the $\text{Mu}-\overline{\text{Mu}}$ conversion process are both controlled by the same flavour-violating couplings that appear in the decays $\mu \rightarrow e\gamma$ and $\mu \rightarrow 3e$. These latter processes provide much stronger experimental limits. As a consequence, after applying all cLFV constraints, we obtain

$$\text{BR}(\text{Mu} \rightarrow e^+e^-) \sim 10^{-18}-10^{-20}, \quad (5.1)$$

far below the current bounds discussed in Sec. 4.3, and still many orders of magnitude below future sensitivities. Likewise, $\text{Mu}-\overline{\text{Mu}}$ conversion, driven by loop-induced box diagrams with heavy neutrinos and dark scalars, leads to

$$|G_{M\overline{M}}| \lesssim 10^{-12}G_F, \quad (5.2)$$

corresponding to $P(\text{Mu} \rightarrow \overline{\text{Mu}}) < 10^{-20}$ and, like the case of Muonium decay, far below future sensitivity. We therefore conclude that Muonium-based searches are not expected to provide competitive probes of this model, whereas cLFV observables in the muon sector remain the most sensitive and promising experimental tests.

6 Conclusions

We have proposed an economical and testable scotogenic model where the smallness of active neutrino masses is explained by a synergy of the linear and inverse seesaw mechanisms, which we name the LISS mechanism. The model extends the SM with a $U(1)'$ gauge symmetry and the discrete $\mathbb{Z}_3 \otimes \mathbb{Z}_4$ symmetries. The key lepton number violating parameters of the LSS (ε) and ISS (μ) are not put in by hand but are dynamically generated at the two-loop level, naturally explaining their smallness. The preserved $\tilde{\mathbb{Z}}_2 \otimes \mathbb{Z}_3$ symmetries (where $\tilde{\mathbb{Z}}_2$ arises from \mathbb{Z}_4 symmetry breaking) that enforce the radiative nature of the seesaw mechanism also guarantee the stability of both scalar and fermionic dark matter candidates, providing a unified framework for two of the most significant shortcomings of the Standard Model. Thanks to the symmetries, our model naturally predicts a fermionic dark matter candidate, i.e., Ψ_R , which is the lightest non trivial Z_3 particle, whose mass arises from a one loop level radiative seesaw mechanism induced by the virtual exchange of the Dark Dirac neutral leptons Ω_L, Ω_R and the Dark scalar fields ξ, χ . In contrast, the dark scalar masses arise at tree level.

Our phenomenological analysis shows that the model is consistent with all current experimental constraints, including neutrino oscillation data, direct searches for heavy neutrinos and Z' bosons, as well as stringent bounds on cLFV processes. An interesting outcome of the analysis is that the inverse seesaw contribution dominates over the linear seesaw one, then implying that atmospheric neutrino mass squared splitting arises from the inverse seesaw mechanism whereas the solar mass squared difference is generated from the linear seesaw. This allows for an explanation of the hierarchy between the atmospheric and solar neutrino mass squared splittings, in addition to the smallness of active neutrino masses, feature not presented in many low-scale seesaw models. Moreover, our parameter-space scan shows a slight preference for the normal ordering, which exhibits a larger allowed region compared to the inverted ordering.

The model predicts cLFV rates—particularly for $\mu \rightarrow e\gamma$, $\mu \rightarrow eee$, and μ - e conversion—that lie within the reach of next-generation experiments such as MEG II, Mu3e, COMET, and Mu2e. We find that these processes are predominantly mediated by scalar loops involving η , since the neutrino contribution is strongly suppressed by the mixing required to satisfy neutrino data. Furthermore, we have explored distinctive predictions for Muonium–antimuonium oscillations and the decay $\text{Mu} \rightarrow e^+e^-$. However, the rates for

these $|\Delta L| = 2$ processes are well below current experimental limits and foreseeable future dedicated searches.

In conclusion, this scotogenic LISS model provides a compelling and verifiable explanation for the origin of neutrino masses, connecting it to dark matter and offering rich phenomenology at both the intensity and energy frontiers. Future work will involve a detailed study of the dark matter candidates and the potential for leptogenesis.

Acknowledgments

AECH is supported by ANID-Chile FONDECYT 1210378, 1241855, ANID PIA/APOYO AFB230003 and ANID – Millennium Science Initiative Program *ICN2019.044*. This project has received funding from the European Union’s Horizon Europe research and innovation programme under the Marie Skłodowska-Curie Staff Exchange grant agreement No 101086085 – ASYMMETRY and support from the IN2P3 (CNRS) Master Project, “Hunting for Heavy Neutral Leptons” (12-PH-0100).

A Anomaly Cancellation

By means of the conditions listed below, we have checked the cancellation of both gauge and gravitational anomalies:

$$A_{[SU(3)_C]^2 U(1)'} = 2 \sum_{i=1}^3 (Q')_{q_{iL}} - \sum_{i=1}^3 \left[(Q')_{u_{iR}} + (Q')_{d_{iR}} \right], \quad (\text{A.1})$$

$$A_{[SU(2)_L]^2 U(1)'} = 2 \sum_{i=1}^3 (Q')_{l_{iL}} + 6 \sum_{i=1}^3 (Q')_{q_{iL}}, \quad (\text{A.2})$$

$$\begin{aligned} A_{[U(1)_Y]^2 U(1)'} &= 2 \sum_{i=1}^3 \left[Y_{l_{iL}}^2 (Q')_{l_{iL}} + 3 Y_{q_{iL}}^2 (Q')_{q_{iL}} \right] \\ &\quad - \sum_{i=1}^3 \left[Y_{l_{iR}}^2 (Q')_{l_{iR}} + 3 Y_{u_{iR}}^2 (Q')_{u_{iR}} + 3 Y_{d_{iR}}^2 (Q')_{d_{iR}} \right], \end{aligned} \quad (\text{A.3})$$

$$\begin{aligned} A_{[U(1)']^2 U(1)_Y} &= 2 \sum_{i=1}^3 \left[Y_{l_{iL}} (Q')_{l_{iL}}^2 + 3 Y_{q_{iL}} (Q')_{q_{iL}}^2 \right] \\ &\quad - \sum_{i=1}^3 \left[Y_{l_{iR}} (Q')_{l_{iR}}^2 + 3 Y_{u_{iR}} (Q')_{u_{iR}}^2 + 3 Y_{d_{iR}} (Q')_{d_{iR}}^2 \right], \end{aligned} \quad (\text{A.4})$$

$$\begin{aligned} A_{[U(1)']^3} &= \sum_{i=1}^3 \left[2 (Q')_{l_{iL}}^3 + 6 (Q')_{q_{iL}}^3 - 3 (Q')_{u_{iR}}^3 - 3 (Q')_{d_{iR}}^3 \right] \\ &\quad - \left\{ \sum_{i=1}^3 (Q')_{l_{iR}}^3 + (Q')_{\nu_R}^3 \right\} \\ &\quad + \left\{ (Q')_{\Psi_L}^3 + (Q')_{\Omega_L}^3 \right\} - \left\{ (Q')_{N_R}^3 + (Q')_{\Psi_R}^3 + (Q')_{\tilde{\Psi}_R}^3 + (Q')_{\Omega_R}^3 \right\}, \end{aligned} \quad (\text{A.5})$$

$$\begin{aligned} A_{[\text{Gravity}]^2 U(1)'} &= \sum_{i=1}^3 \left[2 (Q')_{l_{iL}} + 6 (Q')_{q_{iL}} - 3 (Q')_{u_{iR}} - 3 (Q')_{d_{iR}} \right] \\ &\quad - \left\{ \sum_{i=1}^3 (Q')_{l_{iR}} + (Q')_{\nu_R} \right\} \\ &\quad + \left\{ (Q')_{\Psi_L} + (Q')_{\Omega_L} \right\} - \left\{ (Q')_{N_R} + (Q')_{\Psi_R} + (Q')_{\tilde{\Psi}_R} + (Q')_{\Omega_R} \right\}. \end{aligned} \quad (\text{A.6})$$

The hypercharge Y and $U(1)'$ charges Q' are given in Table 1. In these expressions, A denotes the anomaly coefficient obtained from the triangular diagrams with the gauge bosons corresponding to the groups in the subindices.

B Stability and unitarity conditions

In the regime of very large field values the behavior of the scalar potential is dominated by its quartic interactions. In order to study the stability of the potential, we first extract the quartic part, V_4 , from the full scalar potential. To make our notation more compact, we introduce the following bilinear combinations:

$$\begin{aligned} a &\equiv \phi^\dagger \phi, & b &\equiv \sigma^* \sigma, & c &\equiv \rho^2, \\ d &\equiv \eta^\dagger \eta, & e &\equiv \varphi^* \varphi, & f &\equiv \xi^* \xi, & g &\equiv \chi^* \chi. \end{aligned} \tag{B.1}$$

In addition, note that the term

$$\lambda'_{\phi\eta}(\phi\eta) \left(\eta^\dagger \phi^\dagger \right) \tag{B.2}$$

can be written as $\lambda'_{\phi\eta} |\phi^\dagger \eta|^2$. Furthermore, for the mixed term involving four fields we define

$$h \equiv \xi \sigma^* \chi \rho + \text{h.c.} \tag{B.3}$$

In terms of these bilinears the quartic part of the potential is given by

$$\begin{aligned}
V_4 = & \left(\sqrt{\lambda_\phi} a - \sqrt{\lambda_\sigma} b \right)^2 + \left(\sqrt{\lambda_\phi} a - \sqrt{\lambda_\rho} c \right)^2 + \left(\sqrt{\lambda_\phi} a - \sqrt{\lambda_\eta} d \right)^2 \\
& + \left(\sqrt{\lambda_\phi} a - \sqrt{\lambda_\varphi} e \right)^2 + \left(\sqrt{\lambda_\phi} a - \sqrt{\lambda_\xi} f \right)^2 + \left(\sqrt{\lambda_\phi} a - \sqrt{\lambda_\chi} g \right)^2 \\
& + \left(\sqrt{\lambda_\sigma} b - \sqrt{\lambda_\rho} c \right)^2 + \left(\sqrt{\lambda_\sigma} b - \sqrt{\lambda_\eta} d \right)^2 + \left(\sqrt{\lambda_\sigma} b - \sqrt{\lambda_\varphi} e \right)^2 \\
& + \left(\sqrt{\lambda_\sigma} b - \sqrt{\lambda_\xi} f \right)^2 + \left(\sqrt{\lambda_\sigma} b - \sqrt{\lambda_\chi} g \right)^2 \\
& + \left(\sqrt{\lambda_\rho} c - \sqrt{\lambda_\eta} d \right)^2 + \left(\sqrt{\lambda_\rho} c - \sqrt{\lambda_\varphi} e \right)^2 + \left(\sqrt{\lambda_\rho} c - \sqrt{\lambda_\xi} f \right)^2 \\
& + \left(\sqrt{\lambda_\rho} c - \sqrt{\lambda_\chi} g \right)^2 \\
& + \left(\sqrt{\lambda_\eta} d - \sqrt{\lambda_\varphi} e \right)^2 + \left(\sqrt{\lambda_\eta} d - \sqrt{\lambda_\xi} f \right)^2 + \left(\sqrt{\lambda_\eta} d - \sqrt{\lambda_\chi} g \right)^2 \\
& + \left(\sqrt{\lambda_\varphi} e - \sqrt{\lambda_\xi} f \right)^2 + \left(\sqrt{\lambda_\varphi} e - \sqrt{\lambda_\chi} g \right)^2 + \left(\sqrt{\lambda_\xi} f - \sqrt{\lambda_\chi} g \right)^2 \\
& - 5 \left(\lambda_\phi a^2 + \lambda_\sigma b^2 + \lambda_\rho c^2 + \lambda_\eta d^2 + \lambda_\varphi e^2 + \lambda_\xi f^2 + \lambda_\chi g^2 \right) \\
& + \lambda'_{\phi\eta} |\phi^\dagger \eta|^2 + \lambda_{\xi\sigma\chi\rho} h \\
& + \left(\lambda_{\phi\sigma} - 2\sqrt{\lambda_\phi\lambda_\sigma} \right) ab + \left(\lambda_{\phi\rho} - 2\sqrt{\lambda_\phi\lambda_\rho} \right) ac \\
& + \left(\lambda_{\phi\eta} - 2\sqrt{\lambda_\phi\lambda_\eta} \right) ad + \left(\lambda_{\phi\varphi} - 2\sqrt{\lambda_\phi\lambda_\varphi} \right) ae \\
& + \left(\lambda_{\phi\xi} - 2\sqrt{\lambda_\phi\lambda_\xi} \right) af + \left(\lambda_{\phi\chi} - 2\sqrt{\lambda_\phi\lambda_\chi} \right) ag \\
& + \left(\lambda_{\rho\sigma} - 2\sqrt{\lambda_\rho\lambda_\sigma} \right) bc + \left(\lambda_{\sigma\eta} - 2\sqrt{\lambda_\sigma\lambda_\eta} \right) bd \\
& + \left(\lambda_{\sigma\varphi} - 2\sqrt{\lambda_\sigma\lambda_\varphi} \right) be + \left(\lambda_{\sigma\xi} - 2\sqrt{\lambda_\sigma\lambda_\xi} \right) bf \\
& + \left(\lambda_{\sigma\chi} - 2\sqrt{\lambda_\sigma\lambda_\chi} \right) bg \\
& + \left(\lambda_{\rho\eta} - 2\sqrt{\lambda_\rho\lambda_\eta} \right) cd + \left(\lambda_{\rho\varphi} - 2\sqrt{\lambda_\rho\lambda_\varphi} \right) ce \\
& + \left(\lambda_{\rho\xi} - 2\sqrt{\lambda_\rho\lambda_\xi} \right) cf + \left(\lambda_{\rho\chi} - 2\sqrt{\lambda_\rho\lambda_\chi} \right) cg \\
& + \left(\lambda_{\eta\varphi} - 2\sqrt{\lambda_\eta\lambda_\varphi} \right) de + \left(\lambda_{\eta\xi} - 2\sqrt{\lambda_\eta\lambda_\xi} \right) df \\
& + \left(\lambda_{\eta\chi} - 2\sqrt{\lambda_\eta\lambda_\chi} \right) dg \\
& + \left(\lambda_{\varphi\xi} - 2\sqrt{\lambda_\varphi\lambda_\xi} \right) ef + \left(\lambda_{\varphi\chi} - 2\sqrt{\lambda_\varphi\lambda_\chi} \right) eg \\
& + \left(\lambda_{\xi\chi} - 2\sqrt{\lambda_\xi\lambda_\chi} \right) fg.
\end{aligned} \tag{B.4}$$

Following the procedure outlined in Refs. [150, 151] for stability analysis, we conclude that our scalar potential is stable if the following conditions are met:

$$\lambda_\phi, \lambda_\sigma, \lambda_\rho, \lambda_\eta, \lambda_\varphi, \lambda_\xi, \lambda_\chi, \lambda_{\xi\sigma\chi\rho}, \lambda'_{\phi\eta} \geq 0, \tag{B.5}$$

$$\begin{aligned}
\lambda_{\phi\sigma} + 2\sqrt{\lambda_\phi\lambda_\sigma} &\geq 0, & \lambda_{\phi\rho} + 2\sqrt{\lambda_\phi\lambda_\rho} &\geq 0, & \lambda_{\phi\eta} + 2\sqrt{\lambda_\phi\lambda_\eta} &\geq 0, \\
\lambda_{\phi\varphi} + 2\sqrt{\lambda_\phi\lambda_\varphi} &\geq 0, & \lambda_{\phi\xi} + 2\sqrt{\lambda_\phi\lambda_\xi} &\geq 0, & \lambda_{\phi\chi} + 2\sqrt{\lambda_\phi\lambda_\chi} &\geq 0, \\
\lambda_{\sigma\rho} + 2\sqrt{\lambda_\sigma\lambda_\rho} &\geq 0, & \lambda_{\sigma\eta} + 2\sqrt{\lambda_\sigma\lambda_\eta} &\geq 0, & \lambda_{\sigma\varphi} + 2\sqrt{\lambda_\sigma\lambda_\varphi} &\geq 0, \\
\lambda_{\sigma\xi} + 2\sqrt{\lambda_\sigma\lambda_\xi} &\geq 0, & \lambda_{\sigma\chi} + 2\sqrt{\lambda_\sigma\lambda_\chi} &\geq 0, & \lambda_{\rho\eta} + 2\sqrt{\lambda_\rho\lambda_\eta} &\geq 0, \\
\lambda_{\rho\varphi} + 2\sqrt{\lambda_\rho\lambda_\varphi} &\geq 0, & \lambda_{\rho\xi} + 2\sqrt{\lambda_\rho\lambda_\xi} &\geq 0, & \lambda_{\rho\chi} + 2\sqrt{\lambda_\rho\lambda_\chi} &\geq 0.
\end{aligned} \tag{B.6}$$

In addition to ensuring that the scalar potential is bounded from below, perturbative unitarity at high energies imposes further restrictions on the quartic couplings of the model. these unitary conditions are enforced to prevent scattering amplitudes involving physical scalar particles and longitudinal gauge bosons from increasing excessively with energy. A general amplitude $\mathcal{M}(\theta)$ may be expanded in partial waves as

$$\mathcal{M}(\theta) = 16\pi \sum_{\ell=0}^{\infty} (2\ell+1) a_\ell P_\ell(\cos\theta), \tag{B.7}$$

where $P_\ell(\cos\theta)$ are the Legendre polynomials and a_ℓ denotes the partial wave amplitude of order ℓ . At energies where the scalar field amplitudes become large, the quartic interactions dominate the behavior of the potential. In this regime, one can study the two-body scattering processes involving the scalar fields, applying the equivalence theorem [152–155] to replace the longitudinal gauge boson modes by their corresponding Goldstone bosons. Since the quartic interactions yield constant contributions at high energies, only the s -wave component, a_0 , is significant. The unitarity condition is then enforced by requiring

$$|a_0| < 1, \tag{B.8}$$

or, equivalently, that the eigenvalues of the relevant scattering matrices do not exceed 16π when the conventional normalization is adopted. We will follow a procedure analogous to that in Ref. [41, 151], separating the $2 \rightarrow 2$ scattering processes into those involving electrically neutral pairs and those involving electrically charged pairs.

We will begin with the electrically neutral pairs. Due to the daunting number of scalar fields for clarity, we define the neutral scalar basis by dividing it into two distinct subbases:

$$\mathcal{B}_A = \left(\phi^- \phi^+, \eta^- \eta^+, \frac{hh}{\sqrt{2}}, \frac{\phi_Z \phi_Z}{\sqrt{2}}, \frac{\tilde{\sigma} \tilde{\sigma}}{\sqrt{2}}, \frac{\sigma_{Z'} \sigma_{Z'}}{\sqrt{2}}, \frac{\tilde{\rho} \tilde{\rho}}{\sqrt{2}} \right) \tag{B.9}$$

and

$$\mathcal{B}_I = \left(\frac{\eta_R \eta_R}{\sqrt{2}}, \frac{\eta_I \eta_I}{\sqrt{2}}, \eta_R \eta_I, \frac{\varphi_R \varphi_R}{\sqrt{2}}, \frac{\varphi_I \varphi_I}{\sqrt{2}}, \varphi_R \varphi_I, \frac{\xi_R \xi_R}{\sqrt{2}}, \frac{\xi_I \xi_I}{\sqrt{2}}, \xi_R \xi_I, \frac{\chi_R \chi_R}{\sqrt{2}}, \frac{\chi_I \chi_I}{\sqrt{2}}, \chi_R \chi_I \right). \tag{B.10}$$

where their union forms the complete neutral scalar field basis:

$$\mathcal{B}_N = \mathcal{B}_A \cup \mathcal{B}_I. \tag{B.11}$$

then the neutral scattering matrix, expressed in this basis, adopts the following block form:

$$S_N = \begin{pmatrix} S_A & S_{AI} \\ S_{AI}^T & S_I \end{pmatrix}, \quad (\text{B.12})$$

where the explicit forms of the submatrices S_A , S_{AI} , and S_I in terms of scalar couplings are provided respectively in equations (B.13), (B.14) and (B.15):

$$S_A = \begin{pmatrix} 4\lambda_\phi & \sqrt{2}(\lambda_{\phi\eta} + \lambda'_{\phi\eta}) & \sqrt{2}\lambda_\phi & \sqrt{2}\lambda_\phi & \frac{\lambda_{\phi\sigma}}{\sqrt{2}} & \frac{\lambda_{\phi\sigma}}{\sqrt{2}} & \frac{\lambda_{\phi\rho}}{\sqrt{2}} \\ \sqrt{2}(\lambda_{\phi\eta} + \lambda'_{\phi\eta}) & 4\lambda_\eta & \frac{\lambda_{\phi\eta} + \lambda'_{\phi\eta}}{\sqrt{2}} & \frac{\lambda_{\phi\eta} + \lambda'_{\phi\eta}}{\sqrt{2}} & \frac{\lambda_{\sigma\eta}}{\sqrt{2}} & \frac{\lambda_{\sigma\eta}}{\sqrt{2}} & \frac{\lambda_{\rho\eta}}{\sqrt{2}} \\ \sqrt{2}\lambda_\phi & \frac{\lambda_{\phi\eta} + \lambda'_{\phi\eta}}{\sqrt{2}} & 3\lambda_\phi & \lambda_\phi & \frac{\lambda_{\phi\sigma}}{2} & \frac{\lambda_{\phi\sigma}}{2} & \frac{\lambda_{\phi\rho}}{2} \\ \sqrt{2}\lambda_\phi & \frac{\lambda_{\phi\eta} + \lambda'_{\phi\eta}}{\sqrt{2}} & \lambda_\phi & 3\lambda_\phi & \frac{\lambda_{\phi\sigma}}{2} & \frac{\lambda_{\phi\sigma}}{2} & \frac{\lambda_{\phi\rho}}{2} \\ \frac{\lambda_{\phi\sigma}}{\sqrt{2}} & \frac{\lambda_{\sigma\eta}}{\sqrt{2}} & \frac{\lambda_{\phi\sigma}}{2} & \frac{\lambda_{\phi\sigma}}{2} & 3\lambda_\sigma & \lambda_\sigma & \lambda_{\rho\sigma} \\ \frac{\lambda_{\phi\sigma}}{\sqrt{2}} & \frac{\lambda_{\sigma\eta}}{\sqrt{2}} & \frac{\lambda_{\phi\sigma}}{2} & \frac{\lambda_{\phi\sigma}}{2} & \lambda_\sigma & 3\lambda_\sigma & \lambda_{\rho\sigma} \\ \frac{\lambda_{\phi\rho}}{\sqrt{2}} & \frac{\lambda_{\rho\eta}}{\sqrt{2}} & \frac{\lambda_{\phi\rho}}{2} & \frac{\lambda_{\phi\rho}}{2} & \lambda_{\rho\sigma} & \lambda_{\rho\sigma} & 4\lambda_\rho \end{pmatrix}. \quad (\text{B.13})$$

$$S_I = \begin{pmatrix} 4\lambda_\eta & 0 & \sqrt{2}\lambda_\eta & \frac{\lambda_{\eta\varphi}}{\sqrt{2}} & \frac{\lambda_{\eta\varphi}}{\sqrt{2}} & \frac{\lambda_{\eta\varphi}}{2} & \frac{\lambda_{\eta\xi}}{\sqrt{2}} & \frac{\lambda_{\eta\xi}}{\sqrt{2}} & \frac{\lambda_{\eta\xi}}{2} & \frac{\lambda_{\eta\chi}}{\sqrt{2}} & \frac{\lambda_{\eta\chi}}{\sqrt{2}} & \frac{\lambda_{\eta\chi}}{2} \\ 0 & 4\lambda_\eta & \sqrt{2}\lambda_\eta & \frac{\lambda_{\eta\varphi}}{\sqrt{2}} & \frac{\lambda_{\eta\varphi}}{\sqrt{2}} & \frac{\lambda_{\eta\varphi}}{2} & \frac{\lambda_{\eta\xi}}{\sqrt{2}} & \frac{\lambda_{\eta\xi}}{\sqrt{2}} & \frac{\lambda_{\eta\xi}}{2} & \frac{\lambda_{\eta\chi}}{\sqrt{2}} & \frac{\lambda_{\eta\chi}}{\sqrt{2}} & \frac{\lambda_{\eta\chi}}{2} \\ \sqrt{2}\lambda_\eta & \sqrt{2}\lambda_\eta & 2\lambda_\eta & \frac{\lambda_{\eta\varphi}}{2} & \frac{\lambda_{\eta\varphi}}{2} & 0 & \frac{\lambda_{\eta\xi}}{2} & \frac{\lambda_{\eta\xi}}{2} & 0 & \frac{\lambda_{\eta\chi}}{2} & \frac{\lambda_{\eta\chi}}{2} & 0 \\ \frac{\lambda_{\eta\varphi}}{\sqrt{2}} & \frac{\lambda_{\eta\varphi}}{\sqrt{2}} & \frac{\lambda_{\eta\varphi}}{2} & 3\lambda_\varphi & \lambda_\varphi & \sqrt{2}\lambda_\varphi & \frac{\lambda_{\varphi\xi}}{2} & \frac{\lambda_{\varphi\xi}}{2} & \frac{\lambda_{\varphi\xi}}{\sqrt{2}} & \frac{\lambda_{\varphi\chi}}{\sqrt{2}} & \frac{\lambda_{\varphi\chi}}{\sqrt{2}} & \frac{\lambda_{\varphi\chi}}{2} \\ \frac{\lambda_{\eta\varphi}}{\sqrt{2}} & \frac{\lambda_{\eta\varphi}}{\sqrt{2}} & \frac{\lambda_{\eta\varphi}}{2} & \lambda_\varphi & 3\lambda_\varphi & \sqrt{2}\lambda_\varphi & \frac{\lambda_{\varphi\xi}}{2} & \frac{\lambda_{\varphi\xi}}{2} & \frac{\lambda_{\varphi\xi}}{\sqrt{2}} & \frac{\lambda_{\varphi\chi}}{\sqrt{2}} & \frac{\lambda_{\varphi\chi}}{\sqrt{2}} & \frac{\lambda_{\varphi\chi}}{2} \\ \frac{\lambda_{\eta\varphi}}{2} & \frac{\lambda_{\eta\varphi}}{2} & 0 & \sqrt{2}\lambda_\varphi & \sqrt{2}\lambda_\varphi & 2\lambda_\varphi & \frac{\lambda_{\varphi\xi}}{\sqrt{2}} & \frac{\lambda_{\varphi\xi}}{\sqrt{2}} & 0 & \frac{\lambda_{\varphi\chi}}{2} & \frac{\lambda_{\varphi\chi}}{2} & 0 \\ \frac{\lambda_{\eta\xi}}{\sqrt{2}} & \frac{\lambda_{\eta\xi}}{\sqrt{2}} & \frac{\lambda_{\eta\xi}}{2} & \frac{\lambda_{\varphi\xi}}{2} & \frac{\lambda_{\varphi\xi}}{2} & \frac{\lambda_{\varphi\xi}}{2} & 3\lambda_\xi & \lambda_\xi & \sqrt{2}\lambda_\xi & \frac{\lambda_{\xi\chi}}{\sqrt{2}} & \frac{\lambda_{\xi\chi}}{\sqrt{2}} & \frac{\lambda_{\xi\chi}}{2} \\ \frac{\lambda_{\eta\xi}}{\sqrt{2}} & \frac{\lambda_{\eta\xi}}{\sqrt{2}} & \frac{\lambda_{\eta\xi}}{2} & \frac{\lambda_{\varphi\xi}}{2} & \frac{\lambda_{\varphi\xi}}{2} & \frac{\lambda_{\varphi\xi}}{2} & \lambda_\xi & 3\lambda_\xi & \sqrt{2}\lambda_\xi & \frac{\lambda_{\xi\chi}}{\sqrt{2}} & \frac{\lambda_{\xi\chi}}{\sqrt{2}} & \frac{\lambda_{\xi\chi}}{2} \\ \frac{\lambda_{\eta\xi}}{2} & \frac{\lambda_{\eta\xi}}{2} & 0 & \frac{\lambda_{\varphi\xi}}{\sqrt{2}} & \frac{\lambda_{\varphi\xi}}{\sqrt{2}} & 0 & \sqrt{2}\lambda_\xi & \sqrt{2}\lambda_\xi & 2\lambda_\xi & \frac{\lambda_{\xi\chi}}{2} & \frac{\lambda_{\xi\chi}}{2} & 0 \\ \frac{\lambda_{\eta\chi}}{\sqrt{2}} & \frac{\lambda_{\eta\chi}}{\sqrt{2}} & \frac{\lambda_{\eta\chi}}{2} & \frac{\lambda_{\varphi\chi}}{\sqrt{2}} & \frac{\lambda_{\varphi\chi}}{\sqrt{2}} & \frac{\lambda_{\varphi\chi}}{2} & \frac{\lambda_{\xi\chi}}{\sqrt{2}} & \frac{\lambda_{\xi\chi}}{\sqrt{2}} & \frac{\lambda_{\xi\chi}}{2} & 3\lambda_\chi & \lambda_\chi & \sqrt{2}\lambda_\chi \\ \frac{\lambda_{\eta\chi}}{\sqrt{2}} & \frac{\lambda_{\eta\chi}}{\sqrt{2}} & \frac{\lambda_{\eta\chi}}{2} & \frac{\lambda_{\varphi\chi}}{\sqrt{2}} & \frac{\lambda_{\varphi\chi}}{\sqrt{2}} & \frac{\lambda_{\varphi\chi}}{2} & \frac{\lambda_{\xi\chi}}{\sqrt{2}} & \frac{\lambda_{\xi\chi}}{\sqrt{2}} & \frac{\lambda_{\xi\chi}}{2} & \lambda_\chi & 3\lambda_\chi & \sqrt{2}\lambda_\chi \\ \frac{\lambda_{\eta\chi}}{2} & \frac{\lambda_{\eta\chi}}{2} & 0 & \frac{\lambda_{\varphi\chi}}{2} & \frac{\lambda_{\varphi\chi}}{2} & 0 & \frac{\lambda_{\xi\chi}}{2} & \frac{\lambda_{\xi\chi}}{2} & 0 & \sqrt{2}\lambda_\chi & \sqrt{2}\lambda_\chi & 2\lambda_\chi \end{pmatrix}. \quad (\text{B.14})$$

$$S_{AI} = \begin{pmatrix} \sqrt{2}(\lambda_{\phi\eta} + \lambda'_{\phi\eta}) & \sqrt{2}(\lambda_{\phi\eta} + \lambda'_{\phi\eta}) & (\lambda_{\phi\eta} + \lambda'_{\phi\eta}) & \frac{\lambda_{\phi\varphi}}{\sqrt{2}} & \frac{\lambda_{\phi\varphi}}{\sqrt{2}} & \frac{\lambda_{\phi\varphi}}{2} & \frac{\lambda_{\phi\xi}}{\sqrt{2}} & \frac{\lambda_{\phi\xi}}{\sqrt{2}} & \frac{\lambda_{\phi\xi}}{2} & \frac{\lambda_{\phi\chi}}{\sqrt{2}} & \frac{\lambda_{\phi\chi}}{\sqrt{2}} & \frac{\lambda_{\phi\chi}}{2} \\ \frac{1}{\sqrt{2}}(\lambda_{\phi\eta} + \lambda'_{\phi\eta}) & \frac{1}{\sqrt{2}}(\lambda_{\phi\eta} + \lambda'_{\phi\eta}) & \frac{1}{2}(\lambda_{\phi\eta} + \lambda'_{\phi\eta}) & \frac{\lambda_{\eta\varphi}}{\sqrt{2}} & \frac{\lambda_{\eta\varphi}}{\sqrt{2}} & \frac{\lambda_{\eta\varphi}}{2} & \frac{\lambda_{\eta\xi}}{\sqrt{2}} & \frac{\lambda_{\eta\xi}}{\sqrt{2}} & \frac{\lambda_{\eta\xi}}{2} & \frac{\lambda_{\eta\chi}}{\sqrt{2}} & \frac{\lambda_{\eta\chi}}{\sqrt{2}} & \frac{\lambda_{\eta\chi}}{2} \\ \sqrt{2}\lambda_\phi & \sqrt{2}\lambda_\phi & \lambda_\phi & \frac{\lambda_{\phi\varphi}}{\sqrt{2}} & \frac{\lambda_{\phi\varphi}}{\sqrt{2}} & \frac{\lambda_{\phi\varphi}}{2} & \frac{\lambda_{\phi\xi}}{\sqrt{2}} & \frac{\lambda_{\phi\xi}}{\sqrt{2}} & \frac{\lambda_{\phi\xi}}{2} & \frac{\lambda_{\phi\chi}}{\sqrt{2}} & \frac{\lambda_{\phi\chi}}{\sqrt{2}} & \frac{\lambda_{\phi\chi}}{2} \\ \sqrt{2}\lambda_\phi & \sqrt{2}\lambda_\phi & \lambda_\phi & \frac{\lambda_{\phi\varphi}}{\sqrt{2}} & \frac{\lambda_{\phi\varphi}}{\sqrt{2}} & \frac{\lambda_{\phi\varphi}}{2} & \frac{\lambda_{\phi\xi}}{\sqrt{2}} & \frac{\lambda_{\phi\xi}}{\sqrt{2}} & \frac{\lambda_{\phi\xi}}{2} & \frac{\lambda_{\phi\chi}}{\sqrt{2}} & \frac{\lambda_{\phi\chi}}{\sqrt{2}} & \frac{\lambda_{\phi\chi}}{2} \\ \frac{\lambda_{\sigma\eta}}{\sqrt{2}} & \frac{\lambda_{\sigma\eta}}{\sqrt{2}} & \frac{\lambda_{\sigma\eta}}{2} & \frac{\lambda_{\sigma\varphi}}{\sqrt{2}} & \frac{\lambda_{\sigma\varphi}}{\sqrt{2}} & \frac{\lambda_{\sigma\varphi}}{2} & \frac{\lambda_{\sigma\xi}}{\sqrt{2}} & \frac{\lambda_{\sigma\xi}}{\sqrt{2}} & \frac{\lambda_{\sigma\xi}}{2} & \frac{\lambda_{\sigma\chi}}{\sqrt{2}} & \frac{\lambda_{\sigma\chi}}{\sqrt{2}} & \frac{\lambda_{\sigma\chi}}{2} \\ \frac{\lambda_{\rho\eta}}{\sqrt{2}} & \frac{\lambda_{\rho\eta}}{\sqrt{2}} & \frac{\lambda_{\rho\eta}}{2} & \frac{\lambda_{\rho\varphi}}{\sqrt{2}} & \frac{\lambda_{\rho\varphi}}{\sqrt{2}} & \frac{\lambda_{\rho\varphi}}{2} & \frac{\lambda_{\rho\xi}}{\sqrt{2}} & \frac{\lambda_{\rho\xi}}{\sqrt{2}} & \frac{\lambda_{\rho\xi}}{2} & \frac{\lambda_{\rho\chi}}{\sqrt{2}} & \frac{\lambda_{\rho\chi}}{\sqrt{2}} & \frac{\lambda_{\rho\chi}}{2} \end{pmatrix}. \quad (\text{B.15})$$

Similarly, we introduce the charged scalar basis organized in two subbases:

$$\mathcal{B}_C^{\phi^+} = (\phi^+ h, \phi^+ \phi_Z, \phi^+ \bar{\sigma}, \phi^+ \sigma_{Z'}, \phi^+ \bar{\rho}, \phi^+ \eta_R, \phi^+ \eta_I, \phi^+ \varphi_R, \phi^+ \varphi_I, \phi^+ \xi_R, \phi^+ \xi_I, \phi^+ \chi_R, \phi^+ \chi_I), \quad (\text{B.16})$$

and

$$\mathcal{B}_C^{\eta^-} = (\eta^- h, \eta^- \phi_Z, \eta^- \tilde{\sigma}, \eta^- \sigma_{Z'}, \eta^- \tilde{\rho}, \eta^- \eta_R, \eta^- \eta_I, \eta^- \varphi_R, \eta^- \varphi_I, \eta^- \xi_R, \eta^- \xi_I, \eta^- \chi_R, \eta^- \chi_I). \quad (\text{B.17})$$

Their union forms the complete charged scalar field basis:

$$\mathcal{B}_C = \mathcal{B}_C^{\phi^+} \cup \mathcal{B}_C^{\eta^-}. \quad (\text{B.18})$$

In this charged scalar basis, the corresponding scattering matrix \mathcal{S}_C takes a block-diagonal form:

$$\mathcal{S}_C = \begin{pmatrix} \mathcal{S}_C^{\phi^+} & 0 \\ 0 & \mathcal{S}_C^{\eta^-} \end{pmatrix}, \quad (\text{B.19})$$

where the submatrices $\mathcal{S}_C^{\phi^+}, \mathcal{S}_C^{\eta^-}$ are given by equations (B.20),(B.21) respectively:

$$\mathcal{S}_C^{\phi^+} = \text{diag}\left(2\lambda_\phi, 2\lambda_\phi, \lambda_{\phi\sigma}, \lambda_{\phi\sigma}, \lambda_{\phi\rho}, \lambda_{\phi\eta}, \lambda_{\phi\eta}, \lambda_{\phi\varphi}, \lambda_{\phi\varphi}, \lambda_{\phi\xi}, \lambda_{\phi\xi}, \lambda_{\phi\chi}, \lambda_{\phi\chi}\right) \quad (\text{B.20})$$

$$\mathcal{S}_C^{\eta^-} = \text{diag}\left(2\lambda_\eta, 2\lambda_\eta, \lambda_{\eta\sigma}, \lambda_{\eta\sigma}, \lambda_{\eta\rho}, \lambda_\eta, \lambda_\eta, \lambda_{\eta\varphi}, \lambda_{\eta\varphi}, \lambda_{\eta\xi}, \lambda_{\eta\xi}, \lambda_{\eta\chi}, \lambda_{\eta\chi}\right) \quad (\text{B.21})$$

The unitarity conditions require the moduli of the eigenvalues of \mathcal{S}_N and \mathcal{S}_C to be less than 16π .

C Loop Functions and Form Factors

In this appendix, we collect the explicit expressions for the form factors and loop functions entering the charged lepton flavor violating observables discussed in Section 4.2. The form factors $F_\gamma^{\mu e}, F_Z^{\mu e}, G_\gamma^{\mu e}, F_{\text{Box}}^{\mu e\alpha\alpha}$ are given by [141]:

$$\begin{aligned} F_\gamma^{\mu e} &= \sum_{j=1}^{3+n_S} \mathbf{U}_{ej} \mathbf{U}_{\mu j}^* F_\gamma(x_j), \\ G_\gamma^{\mu e} &= \sum_{j=1}^{3+n_S} \mathbf{U}_{ej} \mathbf{U}_{\mu j}^* G_\gamma(x_j), \\ F_Z^{\mu e} &= \sum_{j,k=1}^{3+n_S} \mathbf{U}_{ej} \mathbf{U}_{\mu k}^* (\delta_{jk} F_Z(x_j) + \mathbf{C}_{jk} G_Z(x_j, x_k) + \mathbf{C}_{jk}^* H_Z(x_j, x_k)), \\ F_{\text{Box}}^{\mu e u u} &= \sum_{j=1}^{3+n_S} \sum_{d_\alpha=d,s,b} \mathbf{U}_{ej} \mathbf{U}_{\mu j}^* V_{d_\alpha} V_{d_\alpha}^* F_{\text{Box}}(x_j, x_{d_\alpha}), \\ F_{\text{Box}}^{\mu e d d} &= \sum_{j=1}^{3+n_S} \sum_{u_\alpha=u,c,t} \mathbf{U}_{ej} \mathbf{U}_{\mu j}^* V_{d_\alpha} V_{d_\alpha}^* F_{\text{XBox}}(x_j, x_{u_\alpha}), \end{aligned}$$

$$F_{\text{Box}}^{\mu e e e} = \sum_{j,k=1}^{3+n_S} \mathbf{U}_{ej} \mathbf{U}_{\mu k}^* (\mathbf{U}_{ej} \mathbf{U}_{ek}^* G_{\text{Box}}(x_j, x_k) - 2 \mathbf{U}_{ej}^* \mathbf{U}_{ek} F_{\text{XBox}}(x_j, x_k)) , \quad (\text{C.1})$$

where $V_{qq'}$ denotes the quark CKM matrix, $\mathbf{C}_{jk} \equiv \sum_{\alpha=e,\mu,\tau} \mathbf{U}_{\alpha j} \mathbf{U}_{\alpha k}^*$, and $x_i = m_{\nu_i}^2/m_W^2$ is the dimensionless mass ratio. In the limit of light masses ($x \ll 1$), the form factors assume the following asymptotic behavior:

$$\begin{aligned} F_{\gamma}^{\mu e} &\xrightarrow{x \ll 1} \sum_{j=1}^{3+n_S} \mathbf{U}_{ej} \mathbf{U}_{\mu j}^* [-x_j] & G_{\gamma}^{\mu e} &\xrightarrow{x \ll 1} \sum_{j=1}^{3+n_S} \mathbf{U}_{ej} \mathbf{U}_{\mu j}^* \left[\frac{x_j}{4} \right] \\ F_Z^{\mu e} &\xrightarrow{x \ll 1} \sum_{j=1}^{3+n_S} \mathbf{U}_{ej} \mathbf{U}_{\mu j}^* \left[x_j \left(\frac{-5}{2} - \ln x_j \right) \right] & F_{\text{Box}}^{\mu e e e} &\xrightarrow{x \ll 1} \sum_{j=1}^{3+n_S} \mathbf{U}_{ej} \mathbf{U}_{\mu j}^* [2 x_j (1 + \ln x_j)] . \end{aligned} \quad (\text{C.2})$$

Finally, the computation of the different amplitudes calls upon the following loop functions [138, 139, 156, 157], entering the form factors of Eq. (C.1):

$$\begin{aligned} F_Z(x) &= -\frac{5x}{2(1-x)} - \frac{5x^2}{2(1-x)^2} \ln x , \\ G_Z(x, y) &= -\frac{1}{2(x-y)} \left[\frac{x^2(1-y)}{1-x} \ln x - \frac{y^2(1-x)}{1-y} \ln y \right] , \\ H_Z(x, y) &= \frac{\sqrt{xy}}{4(x-y)} \left[\frac{x^2-4x}{1-x} \ln x - \frac{y^2-4y}{1-y} \ln y \right] , \\ F_{\gamma}(x) &= \frac{x(7x^2-x-12)}{12(1-x)^3} - \frac{x^2(x^2-10x+12)}{6(1-x)^4} \ln x , \\ G_{\gamma}(x) &= -\frac{x(2x^2+5x-1)}{4(1-x)^3} - \frac{3x^3}{2(1-x)^4} \ln x , \\ F_{\text{Box}}(x, y) &= \frac{1}{x-y} \left\{ \left(4 + \frac{xy}{4} \right) \left[\frac{1}{1-x} + \frac{x^2}{(1-x)^2} \ln x \right] - 2xy \left[\frac{1}{1-x} + \frac{x}{(1-x)^2} \ln x \right] - (x \rightarrow y) \right\} , \\ F_{\text{XBox}}(x, y) &= \frac{-1}{x-y} \left\{ \left(1 + \frac{xy}{4} \right) \left[\frac{1}{1-x} + \frac{x^2}{(1-x)^2} \ln x \right] - 2xy \left[\frac{1}{1-x} + \frac{x}{(1-x)^2} \ln x \right] - (x \rightarrow y) \right\} . \end{aligned} \quad (\text{C.3})$$

In the limit of light masses ($x \ll 1$) and/or degenerate propagators ($x = y$), one has

$$\begin{aligned} F_Z(x) &\xrightarrow{x \ll 1} -\frac{5x}{2} , \\ G_Z(x, x) &= -[x(-1+x-2\ln x)/(2(x-1))] , \quad G_Z(x, x) \xrightarrow{x \ll 1} -\frac{1}{2} x \ln x , \\ H_Z(x, x) &= -\left[\frac{\sqrt{x^2}(4-5x+x^2+(4-2x+x^2)\ln x)}{(4(x-1)^2)} \right] , \\ F_{\gamma}(x) &\xrightarrow{x \ll 1} -x , \\ G_{\gamma}(x) &\xrightarrow{x \ll 1} \frac{x}{4} \\ F_{\text{Box}}(x, x) &= [(-16+31x^2-16x^3+x^4+2x(-16+4x+3x^2)\ln x)/(4(-1+x)^3)] , \end{aligned}$$

$$F_{\text{XBox}}(x, x) = [(-4 + 19x^2 - 16x^3 + x^4 + 2x(-44x + 3x^2) \ln x)/(4(x-1)^3)] . \quad (\text{C.4})$$

D One-Loop LFV Higgs Yukawa and Matching to Scalar Operators

In this Appendix, we connect the fundamental parameters of our model to the effective quark-level scalar couplings $g_{\text{LS}}^{(q)}$ introduced in Eq. (4.9), which enter in $\mu \rightarrow e$ conversion in nuclei.

LFV scalar operators are radiatively generated from the interactions in Eq. (3.1), in particular

$$\mathcal{L} \supset (y_{\Psi})_{i1} \bar{l}_{iL} \eta \Psi_R + \text{h.c.}, \quad (\text{D.1})$$

together with the cubic scalar coupling from the scalar potential,

$$\mathcal{L} \supset -\kappa_{\eta\eta h} h \eta^\dagger \eta, \quad \kappa_{\eta\eta h} \equiv \frac{v_\phi}{\sqrt{2}} (\lambda_{\phi\eta} + \lambda'_{\phi\eta}), \quad (\text{D.2})$$

where $\phi^0 = (v_\phi + h)/\sqrt{2}$.

At one loop level, an effective LFV Higgs Yukawa coupling is induced by the triangle Feynman diagram with internal (η, Ψ_R, η) propagators, as shown in Fig. 6. The required chirality flip occurs on the Ψ_R internal line, then ensuring that the generated effective vertex is purely left-chiral.

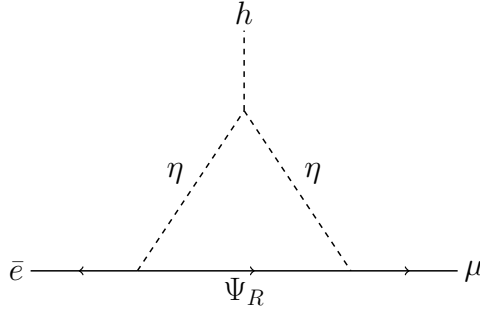


Figure 6: One-loop diagram inducing the $h \bar{e} \mu$ coupling through (η, Ψ_R) exchange.

The loop-induced interaction can be written as

$$\mathcal{L} \supset -\bar{e} (y_{\mu e, L}^h P_L + y_{\mu e, R}^h P_R) \mu h + \text{h.c.}, \quad (\text{D.3})$$

where the coefficients are given by

$$y_{\mu e, L}^h = \frac{(y_{\Psi})_{\mu 1} (y_{\Psi})_{e 1}}{16\pi^2} \kappa_{\eta\eta h} m_{\Psi} C_0(0, 0, m_h^2; m_{\eta}^2, m_{\Psi}^2, m_{\eta}^2), \quad y_{\mu e, R}^h = 0, \quad (\text{D.4})$$

and C_0 is the standard scalar three-point Passarino-Veltman function [158],

$$C_0(0, 0, m_h^2; m_{\eta}^2, m_{\Psi}^2, m_{\eta}^2) = \int_0^1 dx \int_0^{1-x} dy \frac{1}{m_{\eta}^2 + y(m_{\Psi}^2 - m_{\eta}^2) - xy m_h^2}. \quad (\text{D.5})$$

Integrating out the Higgs field at tree level generates the effective four-fermion operator

$$\mathcal{L}_{\text{eff}} \supset - \sum_q \frac{y_{\mu e, L}^h y_q^h}{m_h^2} (\bar{e} P_L \mu)(\bar{q} q) + \text{h.c.}, \quad (\text{D.6})$$

from which the corresponding Wilson coefficients as defined in Eq. (1) of Ref. [135] are identified as

$$g_{LS}^{(q)} = - \frac{\sqrt{2}}{G_F} \frac{y_q^h y_{\mu e, L}^h}{m_h^2}, \quad g_{RS}^{(q)} = 0. \quad (\text{D.7})$$

References

- [1] P. Minkowski, $\mu \rightarrow e\gamma$ at a Rate of One Out of 10^9 Muon Decays?, *Phys. Lett. B* **67** (1977) 421–428.
- [2] T. Yanagida, *Horizontal gauge symmetry and masses of neutrinos*, *Conf. Proc. C* **7902131** (1979) 95–99.
- [3] S. L. Glashow, *The Future of Elementary Particle Physics*, *NATO Sci. Ser. B* **61** (1980) 687.
- [4] R. N. Mohapatra and G. Senjanovic, *Neutrino Mass and Spontaneous Parity Nonconservation*, *Phys. Rev. Lett.* **44** (1980) 912.
- [5] M. Gell-Mann, P. Ramond, and R. Slansky, *Complex Spinors and Unified Theories*, *Conf. Proc. C* **790927** (1979) 315–321, [[arXiv:1306.4669](#)].
- [6] J. Schechter and J. W. F. Valle, *Neutrino Masses in $SU(2) \times U(1)$ Theories*, *Phys. Rev. D* **22** (1980) 2227.
- [7] J. Schechter and J. W. F. Valle, *Neutrino Decay and Spontaneous Violation of Lepton Number*, *Phys. Rev. D* **25** (1982) 774.
- [8] M. Aker et al., *First direct neutrino-mass measurement with sub-eV sensitivity*, [[arXiv:2105.08533](#)].
- [9] D. Wyler and L. Wolfenstein, *Massless Neutrinos in Left-Right Symmetric Models*, *Nucl. Phys. B* **218** (1983) 205–214.
- [10] R. N. Mohapatra and J. W. F. Valle, *Neutrino Mass and Baryon Number Nonconservation in Superstring Models*, *Phys. Rev. D* **34** (1986) 1642.
- [11] M. C. González-García and J. W. F. Valle, *Fast Decaying Neutrinos and Observable Flavor Violation in a New Class of Majoron Models*, *Phys. Lett. B* **216** (1989) 360–366.
- [12] E. K. Akhmedov, M. Lindner, E. Schnapka, and J. W. F. Valle, *Left-right symmetry breaking in NJL approach*, *Phys. Lett. B* **368** (1996) 270–280, [[hep-ph/9507275](#)].
- [13] E. K. Akhmedov, M. Lindner, E. Schnapka, and J. W. F. Valle, *Dynamical left-right symmetry breaking*, *Phys. Rev. D* **53** (1996) 2752–2780, [[hep-ph/9509255](#)].
- [14] M. Malinsky, T. Ohlsson, Z.-z. Xing, and H. Zhang, *Non-unitary neutrino mixing and CP violation in the minimal inverse seesaw model*, *Phys. Lett. B* **679** (2009) 242–248, [[arXiv:0905.2889](#)].

- [15] A. Abada and M. Lucente, *Looking for the minimal inverse seesaw realisation*, *Nucl. Phys. B* **885** (2014) 651–678, [[arXiv:1401.1507](#)].
- [16] S. M. Barr, *A Different seesaw formula for neutrino masses*, *Phys. Rev. Lett.* **92** (2004) 101601, [[hep-ph/0309152](#)].
- [17] M. Malinsky, J. C. Romao, and J. W. F. Valle, *Novel supersymmetric $SO(10)$ seesaw mechanism*, *Phys. Rev. Lett.* **95** (2005) 161801, [[hep-ph/0506296](#)].
- [18] E. Ma, *Radiative inverse seesaw mechanism for nonzero neutrino mass*, *Phys. Rev. D* **80** (2009) 013013, [[arXiv:0904.4450](#)].
- [19] F. Bazzocchi, *Minimal Dynamical Inverse See Saw*, *Phys. Rev. D* **83** (2011) 093009, [[arXiv:1011.6299](#)].
- [20] S. S. C. Law and K. L. McDonald, *Inverse seesaw and dark matter in models with exotic lepton triplets*, *Phys. Lett. B* **713** (2012) 490–494, [[arXiv:1204.2529](#)].
- [21] S. Fraser, E. Ma, and O. Popov, *Scotogenic Inverse Seesaw Model of Neutrino Mass*, *Phys. Lett. B* **737** (2014) 280–282, [[arXiv:1408.4785](#)].
- [22] A. Ahriche, S. M. Boucenna, and S. Nasri, *Dark Radiative Inverse Seesaw Mechanism*, *Phys. Rev. D* **93** (2016), no. 7 075036, [[arXiv:1601.04336](#)].
- [23] A. Das and N. Okada, *Inverse seesaw neutrino signatures at the LHC and ILC*, *Phys. Rev. D* **88** (2013) 113001, [[arXiv:1207.3734](#)].
- [24] A. Das, T. Nomura, H. Okada, and S. Roy, *Generation of a radiative neutrino mass in the linear seesaw framework, charged lepton flavor violation, and dark matter*, *Phys. Rev. D* **96** (2017), no. 7 075001, [[arXiv:1704.02078](#)].
- [25] A. Das, S. Goswami, K. N. Vishnudath, and T. Nomura, *Constraining a general $U(1)'$ inverse seesaw model from vacuum stability, dark matter and collider*, *Phys. Rev. D* **101** (2020), no. 5 055026, [[arXiv:1905.00201](#)].
- [26] A. E. Cárcamo Hernández, R. Martínez, and F. Ochoa, *Fermion masses and mixings in the 3-3-1 model with right-handed neutrinos based on the S_3 flavor symmetry*, *Eur. Phys. J. C* **76** (2016), no. 11 634, [[arXiv:1309.6567](#)].
- [27] A. E. Cárcamo Hernández, S. Kovalenko, J. W. F. Valle, and C. A. Vaquera-Araujo, *Predictive Pati-Salam theory of fermion masses and mixing*, *JHEP* **07** (2017) 118, [[arXiv:1705.06320](#)].
- [28] A. E. Cárcamo Hernández, S. Kovalenko, J. W. F. Valle, and C. A. Vaquera-Araujo, *Neutrino predictions from a left-right symmetric flavored extension of the standard model*, *JHEP* **02** (2019) 065, [[arXiv:1811.03018](#)].
- [29] A. E. Cárcamo Hernández, H. N. Long, and V. V. Vien, *The first $\Delta(27)$ flavor 3-3-1 model with low scale seesaw mechanism*, *Eur. Phys. J. C* **78** (2018), no. 10 804, [[arXiv:1803.01636](#)].
- [30] E. Bertuzzo, S. Jana, P. A. N. Machado, and R. Zukanovich Funchal, *Neutrino Masses and*

- Mixings Dynamically Generated by a Light Dark Sector*, *Phys. Lett. B* **791** (2019) 210–214, [[arXiv:1808.02500](#)].
- [31] S. Mandal, N. Rojas, R. Srivastava, and J. W. F. Valle, *Dark matter as the origin of neutrino mass in the inverse seesaw mechanism*, *Phys. Lett. B* **821** (2021) 136609, [[arXiv:1907.07728](#)].
- [32] A. E. Cárcamo Hernández and S. F. King, *Littlest Inverse Seesaw Model*, *Nucl. Phys. B* **953** (2020) 114950, [[arXiv:1903.02565](#)].
- [33] A. E. Cárcamo Hernández, J. Marchant González, and U. J. Saldaña Salazar, *Viable low-scale model with universal and inverse seesaw mechanisms*, *Phys. Rev. D* **100** (2019), no. 3 035024, [[arXiv:1904.09993](#)].
- [34] A. E. Cárcamo Hernández, Y. Hidalgo Velásquez, and N. A. Pérez-Julve, *A 3-3-1 model with low scale seesaw mechanisms*, *Eur. Phys. J. C* **79** (2019), no. 10 828, [[arXiv:1905.02323](#)].
- [35] A. E. Cárcamo Hernández, D. T. Huong, and H. N. Long, *Minimal model for the fermion flavor structure, mass hierarchy, dark matter, leptogenesis, and the electron and muon anomalous magnetic moments*, *Phys. Rev. D* **102** (2020), no. 5 055002, [[arXiv:1910.12877](#)].
- [36] A. E. Cárcamo Hernández and I. Schmidt, *A renormalizable left-right symmetric model with low scale seesaw mechanisms*, *Nucl. Phys. B* **976** (2022) 115696, [[arXiv:2101.02718](#)].
- [37] A. E. C. Hernández, D. T. Huong, and I. Schmidt, *Universal inverse seesaw mechanism as a source of the SM fermion mass hierarchy*, *Eur. Phys. J. C* **82** (2022), no. 1 63, [[arXiv:2109.12118](#)].
- [38] A. E. Cárcamo Hernández, C. Espinoza, J. C. Gómez-Izquierdo, and M. Mondragón, *Fermion masses and mixings, dark matter, leptogenesis and $g - 2$ muon anomaly in an extended 2HDM with inverse seesaw*, *Eur. Phys. J. Plus* **137** (2022), no. 11 1224, [[arXiv:2104.02730](#)].
- [39] T. Nomura, H. Okada, and P. Sanyal, *A radiatively induced inverse seesaw model with hidden $U(1)$ gauge symmetry*, [arXiv:2103.09494](#).
- [40] A. E. Cárcamo Hernández, H. N. Long, M. L. Mora-Urrutia, N. H. Thao, and V. V. Vien, *Fermion masses and mixings and $g - 2$ muon anomaly in a 3-3-1 model with D_4 family symmetry*, *Eur. Phys. J. C* **82** (2022), no. 8 769, [[arXiv:2104.04559](#)].
- [41] A. Abada, N. Bernal, A. E. C. Hernández, X. Marcano, and G. Piazza, *Gauged inverse seesaw from dark matter*, *Eur. Phys. J. C* **81** (2021), no. 8 758, [[arXiv:2107.02803](#)].
- [42] A. Abada, N. Bernal, A. E. Cárcamo Hernández, S. Kovalenko, and T. B. de Melo, *Three-Loop Inverse Scotogenic Seesaw Models*, [arXiv:2312.14105](#).
- [43] C. Bonilla, A. E. Cárcamo Hernández, B. Saez Diaz, S. Kovalenko, and J. Marchant Gonzalez, *Dark matter from a radiative inverse seesaw majoron model*, *Phys. Lett. B* **847** (2023) 138282, [[arXiv:2306.08453](#)].

- [44] C. Bonilla, A. E. Cárcamo Hernández, S. Kovalenko, H. Lee, R. Pasechnik, and I. Schmidt, *Fermion mass hierarchy in an extended left-right symmetric model*, *JHEP* **12** (2023) 075, [[arXiv:2305.11967](#)].
- [45] V. H. Binh, C. Bonilla, A. E. Cárcamo Hernández, D. T. Huong, V. K. N., H. N. Long, P. N. Thu, and I. Schmidt, *Phenomenology of 3-3-1 models with a radiative inverse seesaw mechanism*, *Phys. Rev. D* **110** (2024), no. 7 075022, [[arXiv:2404.13373](#)].
- [46] A. E. Cárcamo Hernández, D. T. Huong, H. N. Long, and D. Salinas-Arizmendi, *Fermion masses and mixings and charged lepton flavor violation in a 3-3-1 model with inverse seesaw*, *PTEP* **6** (2025) 063, [[arXiv:2412.18550](#)].
- [47] D. T. Huong, A. E. Cárcamo Hernández, H. T. Hung, T. T. Hieu, and N. A. Pérez-Julve, *Extended IDM theory with low scale seesaw mechanisms*, [[arXiv:2502.19488](#)].
- [48] G. Benítez-Irarrázabal, R. B. Balbontín, C. Bonilla, A. E. Cárcamo Hernández, S. Kovalenko, and J. M. González, *A novel two loop inverse seesaw model*, [[arXiv:2512.09063](#)].
- [49] B. S. Balakrishna, A. L. Kagan, and R. N. Mohapatra, *Quark Mixings and Mass Hierarchy From Radiative Corrections*, *Phys. Lett. B* **205** (1988) 345–352.
- [50] E. Ma, *Radiative Quark and Lepton Masses Through Soft Supersymmetry Breaking*, *Phys. Rev. D* **39** (1989) 1922.
- [51] E. Ma, D. Ng, J. T. Pantaleone, and G.-G. Wong, *One Loop Induced Fermion Masses and Exotic Interactions in a Standard Model Context*, *Phys. Rev. D* **40** (1989) 1586.
- [52] E. Ma, *Hierarchical Radiative Quark and Lepton Mass Matrices*, *Phys. Rev. Lett.* **64** (1990) 2866–2869.
- [53] E. Ma, *Pathways to naturally small neutrino masses*, *Phys. Rev. Lett.* **81** (1998) 1171–1174, [[hep-ph/9805219](#)].
- [54] Z.-j. Tao, *Radiative seesaw mechanism at weak scale*, *Phys. Rev. D* **54** (1996) 5693–5697, [[hep-ph/9603309](#)].
- [55] E. Ma, *Verifiable radiative seesaw mechanism of neutrino mass and dark matter*, *Phys. Rev. D* **73** (2006) 077301, [[hep-ph/0601225](#)].
- [56] P.-H. Gu and U. Sarkar, *Radiative Neutrino Mass, Dark Matter and Leptogenesis*, *Phys. Rev. D* **77** (2008) 105031, [[arXiv:0712.2933](#)].
- [57] E. Ma and D. Suematsu, *Fermion Triplet Dark Matter and Radiative Neutrino Mass*, *Mod. Phys. Lett. A* **24** (2009) 583–589, [[arXiv:0809.0942](#)].
- [58] M. Hirsch, R. A. Lineros, S. Morisi, J. Palacio, N. Rojas, and J. W. F. Valle, *WIMP dark matter as radiative neutrino mass messenger*, *JHEP* **10** (2013) 149, [[arXiv:1307.8134](#)].
- [59] A. Aranda and E. Peinado, *A new radiative neutrino mass generation mechanism with higher dimensional scalar representations and custodial symmetry*, *Phys. Lett. B* **754** (2016) 11–13, [[arXiv:1508.01200](#)].

- [60] D. Restrepo, A. Rivera, M. Sánchez-Peláez, O. Zapata, and W. Tangarife, *Radiative Neutrino Masses in the Singlet-Doublet Fermion Dark Matter Model with Scalar Singlets*, *Phys. Rev. D* **92** (2015), no. 1 013005, [[arXiv:1504.07892](#)].
- [61] R. Longas, D. Portillo, D. Restrepo, and O. Zapata, *The Inert Zee Model*, *JHEP* **03** (2016) 162, [[arXiv:1511.01873](#)].
- [62] S. Fraser, E. Ma, and M. Zakeri, *Verifiable Associated Processes from Radiative Lepton Masses with Dark Matter*, *Phys. Rev. D* **93** (2016), no. 11 115019, [[arXiv:1511.07458](#)].
- [63] S. Fraser, C. Kownacki, E. Ma, and O. Popov, *Type II Radiative Seesaw Model of Neutrino Mass with Dark Matter*, *Phys. Rev. D* **93** (2016), no. 1 013021, [[arXiv:1511.06375](#)].
- [64] W. Wang and Z.-L. Han, *Radiative linear seesaw model, dark matter, and $U(1)_{B-L}$* , *Phys. Rev. D* **92** (2015) 095001, [[arXiv:1508.00706](#)].
- [65] C. Arbeláez, A. E. Cárcamo Hernández, S. Kovalenko, and I. Schmidt, *Radiative Seesaw-type Mechanism of Fermion Masses and Non-trivial Quark Mixing*, *Eur. Phys. J. C* **77** (2017), no. 6 422, [[arXiv:1602.03607](#)].
- [66] F. von der Pahlen, G. Palacio, D. Restrepo, and O. Zapata, *Radiative Type III Seesaw Model and its collider phenomenology*, *Phys. Rev. D* **94** (2016), no. 3 033005, [[arXiv:1605.01129](#)].
- [67] T. Nomura and H. Okada, *Radiatively induced Quark and Lepton Mass Model*, *Phys. Lett. B* **761** (2016) 190–196, [[arXiv:1606.09055](#)].
- [68] C. Kownacki and E. Ma, *Gauge $U(1)$ dark symmetry and radiative light fermion masses*, *Phys. Lett. B* **760** (2016) 59–62, [[arXiv:1604.01148](#)].
- [69] T. Nomura and H. Okada, *Loop induced type-II seesaw model and GeV dark matter with $U(1)_{B-L}$ gauge symmetry*, *Phys. Lett. B* **774** (2017) 575–581, [[arXiv:1704.08581](#)].
- [70] T. Nomura and H. Okada, *Radiative neutrino mass in an alternative $U(1)_{B-L}$ gauge symmetry*, *Nucl. Phys. B* **941** (2019) 586–599, [[arXiv:1705.08309](#)].
- [71] N. Bernal, A. E. Cárcamo Hernández, I. de Medeiros Varzielas, and S. Kovalenko, *Fermion masses and mixings and dark matter constraints in a model with radiative seesaw mechanism*, *JHEP* **05** (2018) 053, [[arXiv:1712.02792](#)].
- [72] W. Wang, R. Wang, Z.-L. Han, and J.-Z. Han, *The $B - L$ Scotogenic Models for Dirac Neutrino Masses*, *Eur. Phys. J. C* **77** (2017), no. 12 889, [[arXiv:1705.00414](#)].
- [73] C. Bonilla, S. Centelles-Chuliá, R. Cepedello, E. Peinado, and R. Srivastava, *Dark matter stability and Dirac neutrinos using only Standard Model symmetries*, *Phys. Rev. D* **101** (2020), no. 3 033011, [[arXiv:1812.01599](#)].
- [74] J. Calle, D. Restrepo, C. E. Yaguna, and O. Zapata, *Minimal radiative Dirac neutrino mass models*, *Phys. Rev. D* **99** (2019), no. 7 075008, [[arXiv:1812.05523](#)].
- [75] I. M. Ávila, V. De Romeri, L. Duarte, and J. W. F. Valle, *Phenomenology of scotogenic scalar dark matter*, *Eur. Phys. J. C* **80** (2020), no. 10 908, [[arXiv:1910.08422](#)].

- [76] A. E. Cárcamo Hernández and S. F. King, *Muon anomalies and the $SU(5)$ Yukawa relations*, *Phys. Rev. D* **99** (2019), no. 9 095003, [[arXiv:1803.07367](#)].
- [77] C. Alvarado, C. Bonilla, J. Leite, and J. W. F. Valle, *Phenomenology of fermion dark matter as neutrino mass mediator with gauged $B-L$* , *Phys. Lett. B* **817** (2021) 136292, [[arXiv:2102.07216](#)].
- [78] C. Arbeláez, R. Cepedello, J. C. Helo, M. Hirsch, and S. Kovalenko, *How many 1-loop neutrino mass models are there?*, *JHEP* **08** (2022) 023, [[arXiv:2205.13063](#)].
- [79] R. Cepedello, P. Escribano, and A. Vicente, *Neutrino masses, flavor anomalies, and muon $g-2$ from dark loops*, *Phys. Rev. D* **107** (2023), no. 3 035034, [[arXiv:2209.02730](#)].
- [80] A. E. Cárcamo Hernández, C. Espinoza, J. C. Gómez-Izquierdo, J. Marchant González, and M. Mondragón, *Phenomenology of extended multiHiggs doublet models with S_4 family symmetry*, *Eur. Phys. J. C* **84** (2024), no. 11 1239, [[arXiv:2212.12000](#)].
- [81] J. Leite, S. Sadhukhan, and J. W. F. Valle, *Dynamical scoto-seesaw mechanism with gauged $B-L$ symmetry*, *Phys. Rev. D* **109** (2024), no. 3 035023, [[arXiv:2307.04840](#)].
- [82] A. E. Cárcamo Hernández, L. T. Hue, S. Kovalenko, and H. N. Long, *An extended 3-3-1 model with two scalar triplets and linear seesaw mechanism*, *Eur. Phys. J. Plus* **136** (2021), no. 11 1158, [[arXiv:2001.01748](#)].
- [83] A. E. Cárcamo Hernández, S. Kovalenko, F. S. Queiroz, and Y. S. Villamizar, *An extended 3-3-1 model with radiative linear seesaw mechanism*, *Phys. Lett. B* **829** (2022) 137082, [[arXiv:2105.01731](#)].
- [84] A. E. Cárcamo Hernández, V. K. N., and J. W. F. Valle, *Linear seesaw mechanism from dark sector*, *JHEP* **09** (2023) 046, [[arXiv:2305.02273](#)].
- [85] A. Batra, H. B. Câmara, and F. R. Joaquim, *Dark linear seesaw mechanism*, *Phys. Lett. B* **843** (2023) 138012, [[arXiv:2305.01687](#)].
- [86] A. E. Cárcamo Hernández, Y. H. Velásquez, S. Kovalenko, N. A. Pérez-Julve, and I. Schmidt, *Models of Radiative Linear Seesaw with Electrically Charged Mediators*, *PTEP* **2024** (2024), no. 10 103B02, [[arXiv:2403.05637](#)].
- [87] P. S. B. Dev and A. Pilaftsis, *Minimal Radiative Neutrino Mass Mechanism for Inverse Seesaw Models*, *Phys. Rev. D* **86** (2012) 113001, [[arXiv:1209.4051](#)].
- [88] G. Guo, X.-G. He, and G.-N. Li, *Radiative Two Loop Inverse Seesaw and Dark Matter*, *JHEP* **10** (2012) 044, [[arXiv:1207.6308](#)].
- [89] I. Baldes, N. F. Bell, K. Petraki, and R. R. Volkas, *Two radiative inverse seesaw models, dark matter, and baryogenesis*, *JCAP* **07** (2013) 029, [[arXiv:1304.6162](#)].
- [90] J. C. Gómez-Izquierdo, C. Espinoza, L. E. G. Luna, and M. Mondragón, *Inverse See-Saw Mechanism with S_3 flavor symmetry*, [[arXiv:2411.03392](#)].
- [91] **LZ** Collaboration, J. Aalbers et al., *Dark Matter Search Results from 4.2 Tonne-Years of Exposure of the LUX-ZEPLIN (LZ) Experiment*, *Phys. Rev. Lett.* **135** (2025), no. 1 011802, [[arXiv:2410.17036](#)].

- [92] A. Vilenkin, *Gravitational Field of Vacuum Domain Walls and Strings*, *Phys. Rev. D* **23** (1981) 852–857.
- [93] T. W. B. Kibble, G. Lazarides, and Q. Shafi, *Walls Bounded by Strings*, *Phys. Rev. D* **26** (1982) 435.
- [94] A. Vilenkin, *Cosmic Strings and Domain Walls*, *Phys. Rept.* **121** (1985) 263–315.
- [95] G. Lazarides, M. Reig, Q. Shafi, R. Srivastava, and J. W. F. Valle, *Spontaneous Breaking of Lepton Number and the Cosmological Domain Wall Problem*, *Phys. Rev. Lett.* **122** (2019), no. 15 151301, [[arXiv:1806.11198](#)].
- [96] T. Matsuda, *On the cosmological domain wall problem in supersymmetric models*, *Phys. Lett. B* **436** (1998) 264–268, [[hep-ph/9804409](#)].
- [97] G. R. Dvali and G. Senjanovic, *Is there a domain wall problem?*, *Phys. Rev. Lett.* **74** (1995) 5178–5181, [[hep-ph/9501387](#)].
- [98] S. A. Abel, S. Sarkar, and P. L. White, *On the cosmological domain wall problem for the minimally extended supersymmetric standard model*, *Nucl. Phys. B* **454** (1995) 663–684, [[hep-ph/9506359](#)].
- [99] B. Rai and G. Senjanovic, *Gravity and domain wall problem*, *Phys. Rev. D* **49** (1994) 2729–2733, [[hep-ph/9301240](#)].
- [100] K. Nakayama, F. Takahashi, and N. Yokozaki, *Gravitational waves from domain walls and their implications*, *Phys. Lett. B* **770** (2017) 500–506, [[arXiv:1612.08327](#)].
- [101] K. Saikawa, *A review of gravitational waves from cosmic domain walls*, *Universe* **3** (2017), no. 2 40, [[arXiv:1703.02576](#)].
- [102] A. E. Cárcamo Hernández, D. Restrepo, I. Schmidt, and Ó. Zapata, *Effective Interactions for the SM Fermion Mass Hierarchy and their Possible UV Realization*, *PTEP* **2024** (2024), no. 11 113B01, [[arXiv:2308.10946](#)].
- [103] T. Hiramatsu, M. Kawasaki, and K. Saikawa, *On the estimation of gravitational wave spectrum from cosmic domain walls*, *JCAP* **02** (2014) 031, [[arXiv:1309.5001](#)].
- [104] M. Y. Sassi and G. Moortgat-Pick, *Domain walls in the Two-Higgs-Doublet Model and their charge and CP-violating interactions with Standard Model fermions*, *JHEP* **04** (2024) 101, [[arXiv:2309.12398](#)].
- [105] R. A. Battye, A. Pilaftsis, and D. G. Viatic, *Simulations of Domain Walls in Two Higgs Doublet Models*, *JHEP* **01** (2021) 105, [[arXiv:2006.13273](#)].
- [106] N. Chen, T. Li, Z. Teng, and Y. Wu, *Collapsing domain walls in the two-Higgs-doublet model and deep insights from the EDM*, *JHEP* **10** (2020) 081, [[arXiv:2006.06913](#)].
- [107] **ATLAS** Collaboration, G. Aad et al., *A detailed map of Higgs boson interactions by the ATLAS experiment ten years after the discovery*, *Nature* **607** (2022), no. 7917 52–59, [[arXiv:2207.00092](#)]. [Erratum: *Nature* 612, E24 (2022)].
- [108] **CMS** Collaboration, A. Tumasyan et al., *A portrait of the Higgs boson by the CMS*

- experiment ten years after the discovery.*, *Nature* **607** (2022), no. 7917 60–68, [[arXiv:2207.00043](#)]. [Erratum: *Nature* 623, (2023)].
- [109] **Particle Data Group** Collaboration, S. Navas et al., *Review of particle physics*, *Phys. Rev. D* **110** (2024), no. 3 030001.
- [110] A. Abada, Á. Hernández-Cabezudo, and X. Marcano, *Beta and Neutrinoless Double Beta Decays with KeV Sterile Fermions*, *JHEP* **01** (2019) 041, [[arXiv:1807.01331](#)].
- [111] A. Abada, J. P. Pinheiro, and S. Urrea, *Investigating DUNE oscillations sensitivity to sterile pseudo-Dirac neutrinos*, *JHEP* **11** (2025) 136, [[arXiv:2506.16390](#)].
- [112] Y. Kajiyama, H. Okada, and T. Toma, *Multicomponent dark matter particles in a two-loop neutrino model*, *Phys. Rev. D* **88** (2013), no. 1 015029, [[arXiv:1303.7356](#)].
- [113] J. W. F. Valle, *Neutrinoless Double Beta Decay With Quasi Dirac Neutrinos*, *Phys. Rev. D* **27** (1983) 1672–1674.
- [114] G. Anamiati, M. Hirsch, and E. Nardi, *Quasi-Dirac neutrinos at the LHC*, *JHEP* **10** (2016) 010, [[arXiv:1607.05641](#)].
- [115] C. Arbeláez, C. Dib, K. Monsálvez-Pozo, and I. Schmidt, *Quasi-Dirac neutrinos in the linear seesaw model*, *JHEP* **07** (2021) 154, [[arXiv:2104.08023](#)].
- [116] F. F. Deppisch, N. Desai, and J. W. F. Valle, *Is charged lepton flavor violation a high energy phenomenon?*, *Phys. Rev. D* **89** (2014), no. 5 051302, [[arXiv:1308.6789](#)].
- [117] A. Abada and A. M. Teixeira, *Heavy neutral leptons and high-intensity observables*, *Front. in Phys.* **6** (2018) 142, [[arXiv:1812.08062](#)].
- [118] E. Fernandez-Martinez, J. Hernandez-Garcia, and J. Lopez-Pavon, *Global constraints on heavy neutrino mixing*, *JHEP* **08** (2016) 033, [[arXiv:1605.08774](#)].
- [119] **LEP, ALEPH, DELPHI, L3, LEP Electroweak Working Group, SLD Electroweak Group, SLD Heavy Flavour Group, OPAL** Collaboration, *A Combination of preliminary electroweak measurements and constraints on the standard model*, [hep-ex/0412015](#).
- [120] M. Carena, A. Daleo, B. A. Dobrescu, and T. M. P. Tait, *Z' gauge bosons at the Tevatron*, *Phys. Rev. D* **70** (2004) 093009, [[hep-ph/0408098](#)].
- [121] A. Das, P. S. B. Dev, Y. Hosotani, and S. Mandal, *Probing the minimal U(1)X model at future electron-positron colliders via fermion pair-production channels*, *Phys. Rev. D* **105** (2022), no. 11 115030, [[arXiv:2104.10902](#)].
- [122] **ATLAS** Collaboration, G. Aad et al., *Search for high-mass dilepton resonances using 139 fb⁻¹ of pp collision data collected at $\sqrt{s} = 13$ TeV with the ATLAS detector*, *Phys. Lett. B* **796** (2019) 68–87, [[arXiv:1903.06248](#)].
- [123] **CMS** Collaboration, A. M. Sirunyan et al., *Search for resonant and nonresonant new phenomena in high-mass dilepton final states at $\sqrt{s} = 13$ TeV*, *JHEP* **07** (2021) 208, [[arXiv:2103.02708](#)].

- [124] B. Dutta, G. Palacio, J. D. Ruiz-Alvarez, and D. Restrepo, *Vector Boson Fusion in the Inert Doublet Model*, *Phys. Rev. D* **97** (2018), no. 5 055045, [[arXiv:1709.09796](#)].
- [125] A. Alves, A. Berlin, S. Profumo, and F. S. Queiroz, *Dark Matter Complementarity and the Z' Portal*, *Phys. Rev. D* **92** (2015), no. 8 083004, [[arXiv:1501.03490](#)].
- [126] P. Langacker and D. London, *Lepton Number Violation and Massless Nonorthogonal Neutrinos*, *Phys. Rev. D* **38** (1988) 907.
- [127] L. Lavoura, *General formulae for $f(1) \rightarrow f(2) + \gamma$* , *Eur. Phys. J. C* **29** (2003) 191–195, [[hep-ph/0302221](#)].
- [128] L. T. Hue, L. D. Ninh, T. T. Thuc, and N. T. T. Dat, *Exact one-loop results for $l_i \rightarrow l_j \gamma$ in 3-3-1 models*, *Eur. Phys. J. C* **78** (2018), no. 2 128, [[arXiv:1708.09723](#)].
- [129] A. Batra, P. Bharadwaj, S. Mandal, R. Srivastava, and J. W. F. Valle, *Phenomenology of the simplest linear seesaw mechanism*, *JHEP* **07** (2023) 221, [[arXiv:2305.00994](#)].
- [130] E. Ma and M. Raidal, *Neutrino mass, muon anomalous magnetic moment, and lepton flavor nonconservation*, *Phys. Rev. Lett.* **87** (2001) 011802, [[hep-ph/0102255](#)]. [Erratum: *Phys.Rev.Lett.* 87, 159901 (2001)].
- [131] T. Toma and A. Vicente, *Lepton Flavor Violation in the Scotogenic Model*, *JHEP* **01** (2014) 160, [[arXiv:1312.2840](#)].
- [132] A. Vicente and C. E. Yaguna, *Probing the scotogenic model with lepton flavor violating processes*, *JHEP* **02** (2015) 144, [[arXiv:1412.2545](#)].
- [133] M. Lindner, M. Platscher, and F. S. Queiroz, *A Call for New Physics : The Muon Anomalous Magnetic Moment and Lepton Flavor Violation*, *Phys. Rept.* **731** (2018) 1–82, [[arXiv:1610.06587](#)].
- [134] A. Abada, N. Bernal, A. E. Cárcamo Hernández, S. Kovalenko, T. B. de Melo, and T. Toma, *Phenomenological and cosmological implications of a scotogenic three-loop neutrino mass model*, *JHEP* **03** (2023) 035, [[arXiv:2212.06852](#)].
- [135] R. Kitano, M. Koike, and Y. Okada, *Detailed calculation of lepton flavor violating muon electron conversion rate for various nuclei*, *Phys. Rev. D* **66** (2002) 096002, [[hep-ph/0203110](#)]. [Erratum: *Phys.Rev.D* 76, 059902 (2007)].
- [136] T. S. Kosmas, S. Kovalenko, and I. Schmidt, *Nuclear muon- e - conversion in strange quark sea*, *Phys. Lett. B* **511** (2001) 203, [[hep-ph/0102101](#)].
- [137] Y. Kuno and Y. Okada, *Muon decay and physics beyond the standard model*, *Rev. Mod. Phys.* **73** (2001) 151–202, [[hep-ph/9909265](#)].
- [138] A. Ilakovac and A. Pilaftsis, *Flavor violating charged lepton decays in seesaw-type models*, *Nucl. Phys. B* **437** (1995) 491, [[hep-ph/9403398](#)].
- [139] R. Alonso, M. Dhen, M. B. Gavela, and T. Hambye, *Muon conversion to electron in nuclei in type-I seesaw models*, *JHEP* **01** (2013) 118, [[arXiv:1209.2679](#)].
- [140] B. Pontecorvo, *Mesonium and Antimesonium*, *Sov. Phys. JETP* **6** (1958) 429–431.

- [141] G. Cvetič, C. O. Dib, C.-S. Kim, and J. Kim, *Lepton flavor violation in muonium decay and muon colliders in models with heavy neutrinos*, *Phys. Rev. D* **74** (2006) 093011, [[hep-ph/0608203](#)].
- [142] G. Feinberg and S. Weinberg, *Conversion of Muonium into Antimuonium*, *Phys. Rev.* **123** (1961) 1439–1443.
- [143] T. Fukuyama, Y. Mimura, and Y. Uesaka, *Models of the muonium to antimuonium transition*, *Phys. Rev. D* **105** (2022), no. 1 015026, [[arXiv:2108.10736](#)].
- [144] L. Willmann et al., *New bounds from searching for muonium to anti-muonium conversion*, *Phys. Rev. Lett.* **82** (1999) 49–52, [[hep-ex/9807011](#)].
- [145] S. N. Gninenko, N. V. Krasnikov, and V. A. Matveev, *Invisible Decay of Muonium: Tests of the Standard Model and Searches for New Physics*, *Phys. Rev. D* **87** (2013), no. 1 015016, [[arXiv:1209.0060](#)].
- [146] J. Tang and et al., *Search for muonium to antimuonium conversion*, . MACE Working Group Collaboration. Available at https://www.snowmass21.org/docs/files/summaries/RF/SNOWMASS21-RF5_RF0_Jian_Tang-126.pdf.
- [147] N. Kawamura, R. Kitamura, H. Yasuda, M. Otani, Y. Nakazawa, H. Iinuma, and T. Mibe, *A New Approach for Muonium–Antimuonium Conversion Search*, *JPS Conf. Proc.* **33** (2021) 011120.
- [148] I. Esteban, M. C. Gonzalez-Garcia, M. Maltoni, I. Martinez-Soler, J. P. Pinheiro, and T. Schwetz, *NuFit-6.0: updated global analysis of three-flavor neutrino oscillations*, *JHEP* **12** (2024) 216, [[arXiv:2410.05380](#)].
- [149] E. Fernández-Martínez, M. González-López, J. Hernández-García, M. Hostert, and J. López-Pavón, *Effective portals to heavy neutral leptons*, *Journal of High Energy Physics* **2023** (Sept., 2023).
- [150] M. Maniatis, A. von Manteuffel, O. Nachtmann, and F. Nagel, *Stability and symmetry breaking in the general two-Higgs-doublet model*, *Eur. Phys. J. C* **48** (2006) 805–823, [[hep-ph/0605184](#)].
- [151] G. Bhattacharyya and D. Das, *Scalar sector of two-Higgs-doublet models: A minireview*, *Pramana* **87** (2016), no. 3 40, [[arXiv:1507.06424](#)].
- [152] J. M. Cornwall, D. N. Levin, and G. Tiktopoulos, *Derivation of Gauge Invariance from High-Energy Unitarity Bounds on the s Matrix*, *Phys. Rev. D* **10** (1974) 1145. [Erratum: *Phys.Rev.D* 11, 972 (1975)].
- [153] C. E. Vayonakis, *Born Helicity Amplitudes and Cross-Sections in Nonabelian Gauge Theories*, *Lett. Nuovo Cim.* **17** (1976) 383.
- [154] B. W. Lee, C. Quigg, and H. B. Thacker, *Weak Interactions at Very High-Energies: The Role of the Higgs Boson Mass*, *Phys. Rev. D* **16** (1977) 1519.
- [155] G. J. Gounaris, R. Kogerler, and H. Neufeld, *Relationship Between Longitudinally Polarized Vector Bosons and their Unphysical Scalar Partners*, *Phys. Rev. D* **34** (1986) 3257.

- [156] E. Ma and A. Pramudita, *Flavor Changing Effective Neutral Current Couplings in the Weinberg-Salam Model*, *Phys. Rev. D* **22** (1980) 214.
- [157] M. Gronau, C. N. Leung, and J. L. Rosner, *Extending Limits on Neutral Heavy Leptons*, *Phys. Rev. D* **29** (1984) 2539.
- [158] G. 't Hooft and M. J. G. Veltman, *Scalar One Loop Integrals*, *Nucl. Phys. B* **153** (1979) 365–401.